Cell Reports

Article

# Perlecan (*HSPG2*) promotes structural, contractile, and metabolic development of human cardiomyocytes

## Graphical abstract

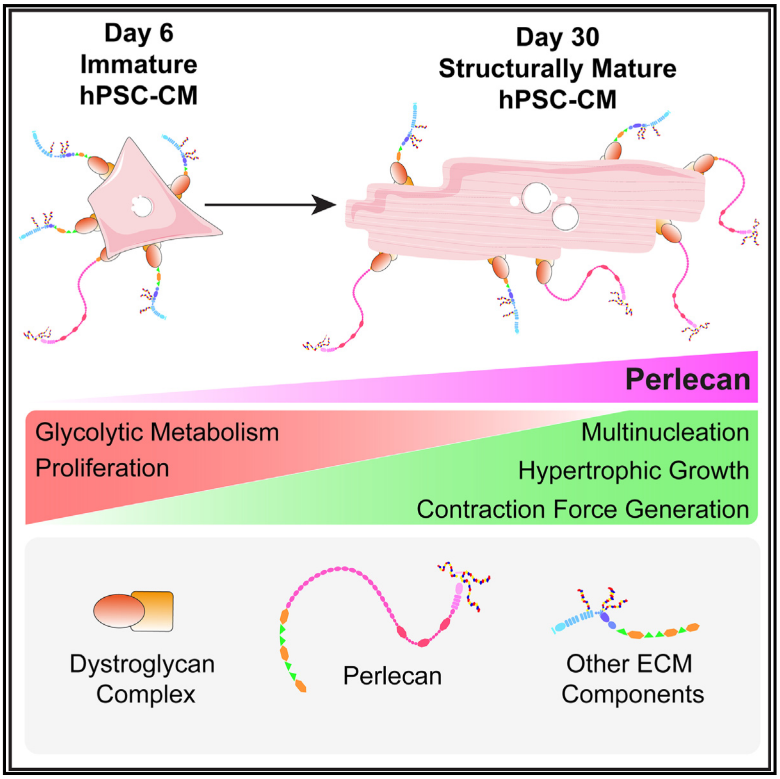

## Highlights

- Perlecan expression increases during cardiomyocyte differentiation and binds dystroglycan
- Perlecan-deficient cardiomyocytes show immature gene expression and metabolic profiles
- Perlecan-deficient 3D cardiac tissues show reduced tissue thickness and force generation
- Perlecan peptide substrates increase nucleation and hypertrophic growth of cardiomyocytes

## Authors

Benjamin B. Johnson,
Marie-Victoire Cosson,
Lorenza I. Tsansizi, ...,
Stuart A. Rushworth, Andreia S. Bernardo,
James G.W. Smith

## Correspondence

a.bernardo@imperial.ac.uk (A.S.B.),
j.g.smith@uea.ac.uk (J.G.W.S.)

## In brief

Johnson et al. demonstrate that perlecan, a proteoglycan found in the extracellular matrix, promotes hypertrophic growth and cardiomyocyte maturation. Perlecan haploinsufficiency leads to increased glycolysis reliance, increased cardiomyocyte proliferation, and reduced α-actinin and contraction-amplitude. Moreover, they show that perlecan binds the dystroglycan complex with expression increasing over time, likely facilitating cardiomyocyte maturation.

Johnson et al., 2024, Cell Reports *43*, 113668
January 23, 2024 © 2024 The Authors.
https://doi.org/10.1016/j.celrep.2023.113668

CellPress

Cell Reports

CellPress
OPEN ACCESS

Article

# Perlecan (*HSPG2*) promotes structural, contractile, and metabolic development of human cardiomyocytes

Benjamin B. Johnson,[1] Marie-Victoire Cosson,[2,3,9] Lorenza I. Tsansizi,[2,3,9] Terri L. Holmes,[1] Tegan Gilmore,[2] Katherine Hampton,[1] Ok-Ryul Song,[2,4] Nguyen T.N. Vo,[5] Aishah Nasir,[5] Alzbeta Chabronova,[6] Chris Denning,[5] Mandy J. Peffers,[6] Catherine L.R. Merry,[5,7] John Whitelock,[5,8] Linda Troeberg,[1] Stuart A. Rushworth,[1] Andreia S. Bernardo,[2,3,*] and James G.W. Smith[1,10,*]

[1]Centre for Metabolic Health, Norwich Medical School, University of East Anglia, Norwich Research Park, Norwich NR4 7UQ, UK
[2]The Francis Crick Institute, London NW1 1AT, UK
[3]NHLI, Imperial College London, London, UK
[4]High-Throughput Screening Science Technology Platform, The Francis Crick Institute, London NW1 1AT, UK
[5]School of Medicine, Regenerating and Modelling Tissues, Biodiscovery Institute, University Park, University of Nottingham, Nottingham NG7 2RD, UK
[6]Institute of Life Course and Medical Sciences, William Henry Duncan Building, 6 West Derby Street, Liverpool L7 8TX, UK
[7]Department of Medical Biochemistry and Microbiology, Uppsala University, Uppsala, Sweden
[8]Graduate School of Biomedical Engineering, University of New South Wales, Sydney, NSW 2052, Australia
[9]These authors contributed equally
[10]Lead contact
*Correspondence: a.bernardo@imperial.ac.uk (A.S.B.), j.g.smith@uea.ac.uk (J.G.W.S.)
https://doi.org/10.1016/j.celrep.2023.113668

## SUMMARY

Perlecan (*HSPG2*), a heparan sulfate proteoglycan similar to agrin, is key for extracellular matrix (ECM) maturation and stabilization. Although crucial for cardiac development, its role remains elusive. We show that perlecan expression increases as cardiomyocytes mature *in vivo* and during human pluripotent stem cell differentiation to cardiomyocytes (hPSC-CMs). Perlecan-haploinsufficient hPSCs (*HSPG2*$^{+/-}$) differentiate efficiently, but late-stage CMs have structural, contractile, metabolic, and ECM gene dysregulation. In keeping with this, late-stage *HSPG2*$^{+/-}$ hPSC-CMs have immature features, including reduced α-actinin expression and increased glycolytic metabolism and proliferation. Moreover, perlecan-haploinsufficient engineered heart tissues have reduced tissue thickness and force generation. Conversely, hPSC-CMs grown on a perlecan-peptide substrate are enlarged and display increased nucleation, typical of hypertrophic growth. Together, perlecan appears to play the opposite role of agrin, promoting cellular maturation rather than hyperplasia and proliferation. Perlecan signaling is likely mediated via its binding to the dystroglycan complex. Targeting perlecan-dependent signaling may help reverse the phenotypic switch common to heart failure.

## INTRODUCTION

Cardiomyocytes, the contractile cells of the heart, are capable of initiating and generating the forces required for healthy cardiac function. Although cardiomyocytes first develop during embryonic cardiogenesis, they continue to undergo postnatal phenotypic changes in a development phase known as maturation.[1] During maturation, cardiomyocytes withdraw from the cell cycle and switch from proliferative, hyperplastic growth to non-proliferative, hypertrophic growth, which typically leads to nuclear ploidy and multinucleation in mammals.[2–5] Postnatal cardiomyocyte division is very limited in mammals,[6] while zebrafish fish hearts, being composed almost exclusively of diploid cells, are still able to proliferate.[7–9] To explain the regenerative capacity of fish hearts, a model has been proposed where cells in these hearts undergo a “phenotypic switch,” enabling cardiomyocytes to dedifferentiate and re-enter the cell cycle.[10]

The heart extracellular matrix (ECM), comprising a complex network of fibrillar collagens and non-fibrillar proteoglycans and glycoproteins, plays a key role in cardiomyocyte phenotypic switching.[11] Specifically, the binding of ECM components and soluble mediators (e.g., growth factors) to transmembrane cell surface receptors can activate signaling pathways, directly inducing a cardiomyocyte phenotypic switch.[12] The ECM also tightly regulates cellular processes throughout heart development and disease,[11,13] primarily through the binding of numerous growth factors and cytokines to ECM components, which are subsequently released in response to physiological or pathological cues.[11]

Agrin is an ECM heparan sulfate proteoglycan (HSPG) known to influence cardiomyocyte proliferation and phenotypic

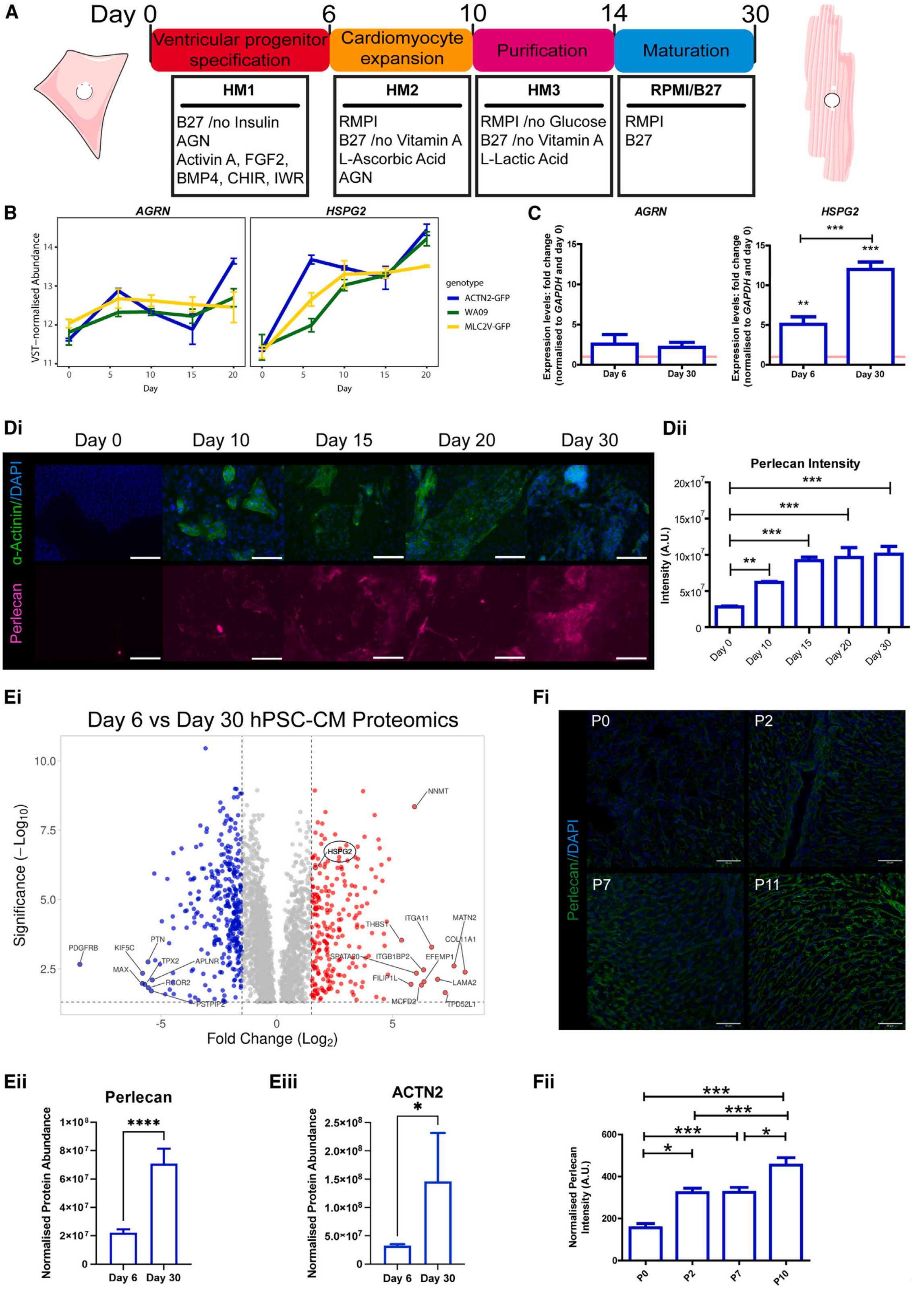

(legend on next page)

switching.[14] It does so via binding to the dystrophin glycoprotein complex (DGC), which links the actin cytoskeleton to the surrounding ECM.[15] Although agrin is enriched in neonatal ECM, it is downregulated at postnatal day 7 (P7), as cardiomyocytes stop proliferating and switch to hypertrophic expansion.[2,16] The regulation of the agrin-DGC axis remains, however, largely undetermined. For example, how is agrin-DGC binding controlled postnatally, especially since there is little/no proliferation after P7? What role is played by other ECM DGC-binding components?[17] Is it possible that additional DGC-binding factors may increase postnatally, outcompeting agrin or having higher affinity than agrin for DGC?[17] A potential candidate for this role in cardiomyocytes is perlecan (*HSPG2*), which exhibits significant structural similarity with agrin and shares the C-terminal laminin-globular DGC-binding domain.[18] During neuronal development, agrin and perlecan compete for DGC binding, presenting differentially bound growth factors in both a calcium- and heparin-sensitive manner.[19] Moreover, the C terminus of perlecan is reported to bind the DGC with greater affinity than the C terminus of agrin.[15,20]

During mouse heart development, perlecan is localized to either the basal surface or the basement membrane of the myocardium and endocardium.[21] Perlecan expression is also seen in cardiomyocytes from gestational week 8 in humans.[22] Perlecan deficiency in mice is often lethal, with widespread cardiac defects observed.[23–25] Moreover, following myocardial infarction, perlecan increases in the infarcted and border regions, with perlecan-deficient mice showing increased susceptibility to cardiac dysfunction upon cryoinjury.[25,26] As such, perlecan is known to be crucial for cardiac development and for heart injury resolution, but a direct role for perlecan in cardiomyocyte postnatal maturation or in phenotypic switching has not been studied previously.

Here, we used human pluripotent stem cells (hPSCs) coupled to a protocol that generates left-ventricle-like cardiomyocytes with hallmarks of neonatal-like maturity[27] to investigate the expression and function of perlecan during development and early maturation. To understand the role of perlecan in this context, perlecan-haploinsufficient hPSCs were generated. Data show that perlecan expression levels are increased during the maturation stage of differentiation, coinciding with the onset of transcriptomic and functional changes seen in perlecan haploinsufficient cardiomyocytes. These changes included increased proliferation, reduced contraction force, and an immature metabolic profile within *HSPG2*$^{+/-}$ hPSC cardiomyocytes (CMs). In addition, maturation of wild-type hPSC-CMs on a perlecan peptide (PER-P)-coated substrate increased CM size and promoted multinucleation, characteristic of increased hypertrophic growth. We further show that perlecan binds the dytroglycan complex, its likely intracellular signaling mediator. Together, these data suggest that perlecan signaling has a regulatory role during the maturation stage of CM development, promoting the developmental switch to hypertrophic growth. As such, exploiting perlecan signaling has the potential for improving CM functionality, especially to counteract the detrimental phenotypic switching typical of many disorders or to promote myocardial regeneration.

## RESULTS

### Perlecan expression increases during the maturation stage of hPSC-CM differentiation and in postnatal mouse CMs from P7/P10

The mEGFP-tagged *ACTN2* wild-type hPSC line (AICS-0075-085, herein referred to as ACTN2-GFP or wild type [WT]) was induced to differentiate into CMs using the method outlined in Figure 1A, which leads to the generation of left ventricle CMs with increased mature properties.[27] To understand the dynamic changes in both *HSPG2* and *AGRN* expression, transcriptomic analysis was performed on cells at key transition points during differentiation, and the results were compared between this line and two other WT lines (WA09 and AICS-0060-027-MLC2V-GFP) we had previously studied.[27] Compared to undifferentiated hPSCs (day 0), the expression of both *HSPG2* and *AGRN* increased in early CMs (day 6), but while it remained stable thereafter for *AGRN*, it increased further during the maturation stage for *HSPG2* (Figure 1B). Overall, the magnitude of transcriptional change was greater for *HSPG2* than *AGRN* at days 20/30 of differentiation, and these results were confirmed by real-time PCR analysis (Figures 1B and 1C).

Next, we performed transcript analysis of both *HSPG2* and *AGRN* to understand which variant(s) contribute to their global expression changes (Figures S1A–S1C). Only one *AGRN* transcript variant increased between days 0 and 6 (ENST00000379370.7, AGRN-201-c), while the others remained unchanged over time in culture (Figure S1B). On the other hand, we found that the

**Figure 1. Perlecan and agrin expression during hPSC-CM differentiation**

(A) Schematic of CM differentiation protocol with differential stages and key media compositions labeled. Stem cells are specified into ventricular progenitors (days 0–6), early spontaneous contracting CMs (day 6), continue into proliferative CM stage (days 6–10), followed by metabolic selection (days 10–14), and finally *in vitro* maturation (days 14–30).

(B and C) Perlecan (*HSPG2*) and agrin (*AGRN*) transcript expression during hPSC-CM differentiation determined through (B) VST-normalized counts following deSeq2 normalization of RNA sequencing analysis and (C) SYBR Green real-time PCR (n = 3).

(Di) Representative fluorescent images of perlecan immunocytochemistry during hPSC-CM differentiation shown in purple, with α-actinin (green) and DAPI nuclei (blue) shown. Scale bars: 150 μm.

(Dii) Quantification of immunocytochemistry-normalized intensity.

(E) Label-free liquid chromatography-tandem mass spectrometry (LC-MS/MS) analysis between day 6 and 30 hPSC-CMs showing differentially expressed proteins (DEPs) in (Ei) volcano plot with positive (red) and negative (blue) log fold changes, (Eii) normalized perlecan protein abundance, and (Eiii) normalized α-actinin (ACTN2) abundance.

(F) Immunohistochemistry of perlecan expression in murine heart sections from postnatal day 0 (P0) to P10.

(Fi) Representative fluorescent images showing perlecan in green and DAPI in blue. Scale bar: 50 μm.

(Fii) Quantification of normalized perlecan intensity. Data, mean ± SD. Significance was determined by one-way ANOVA or a t test, $^{*}p < 0.05$, $^{**}p < 0.01$, $^{***}p < 0.001$.

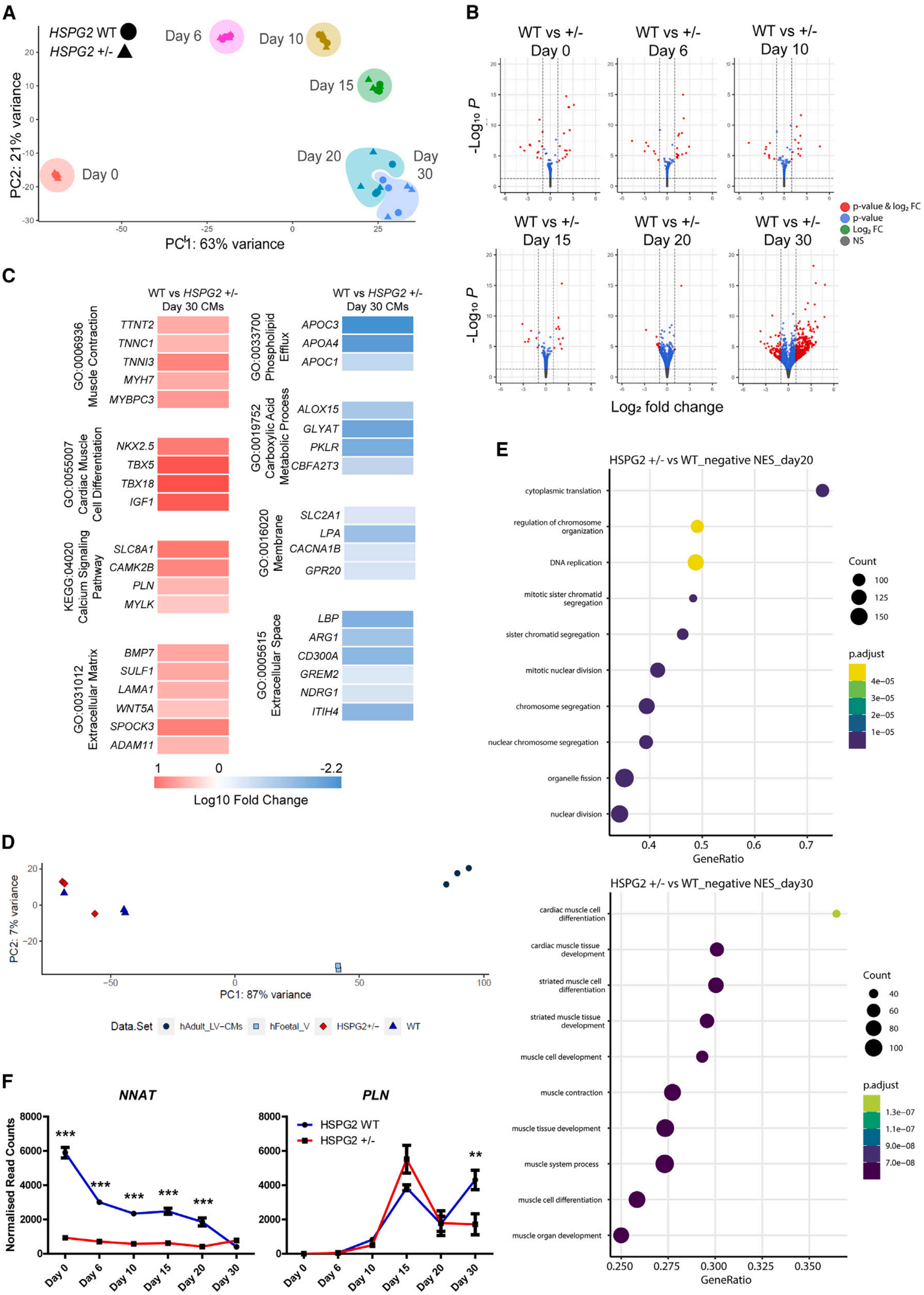

*(legend on next page)*

full-length *HSPG2* transcript (ENST00000374695, HSPG2-203-c) increased sharply over time in culture and was the most abundant. Four additional transcripts were expressed at high levels (8–14 variance-stabilizing transformation [VST]-normalized expression), and their expression also increased over time in culture, including a C-terminal-specific transcript (ENST00000486901, HSPG2-211), the second most abundant transcript (Figure S1Ci). The remaining transcript variants remained unchanged during the differentiation, suggesting that not all *HSPG2* transcripts are specific to CMs (Figure S1Cii).

To determine if transcriptomic expression changes translated into differences in protein abundance, cells were collected at different time points for immunostaining and western blot. Immunostaining showed a consistent and significant increase in perlecan abundance from day 10 of differentiation (Figures 1Di and 1Dii). Western blot analysis using a polyclonal antibody confirmed this trend, with perlecan expression increasing during hPSC differentiation (Figure S1Eii). Unbiased proteomic analysis between days 6 and 30 confirmed that perlecan protein expression increased 3.2-fold for hPSC-CMs (Figures 1Ei and Eii), as was also the case for $\alpha$-actinin (Figure 1Eiii). On the other hand, agrin expression was mostly unchanged in CMs (Figures S1D and S1Ei).

Analysis of mouse heart sections from P0 to P10 further showed that perlecan protein expression increased postnatally, confirming a correlation between maturation and perlecan expression upregulation (Figures 1Fi and 1Fii). Interestingly, western blot analysis showed that while some agrin variants are reduced during the first days of postnatal life, in keeping with a previous report,[14] the overall levels remain unchanged (Figure S1Fi). On the other hand, two small perlecan forms increased in the same period, confirming the trend observed by immunostaining (Figure S1Fii).

Together, these data showed that perlecan expression increases during hPSC-CM differentiation (and postnatally in mice), with the highest levels seen in more mature cultures, suggesting it may contribute to CM maturation, unlike agrin, which is mostly associated with CM proliferation rather than maturation.

## Perlecan-deficient hPSC-CMs show altered transcriptomic profile during maturation

To assess the role of perlecan in CM differentiation and ascertain its potential involvement in cellular maturation, we used CRISPR-Cas9 to produce a heterozygous (*HSPG2*$^{+/-}$) hPSC line with ~50% gene expression, characteristic of haploinsufficiency; the ACTN2-GFP line was the parental line (Figures S2A–S2C). These haploinsufficient cells retained their pluripotent characteristics, and their growth was not affected (Figures S2D–S2F). Transcriptomic analysis of the parental and *HSPG2*$^{+/-}$ lines as they differentiated to CMs revealed the greatest number of differentially expressed genes (DEGs) was observed between days 0 and 6 (Figures S3A and S3B). Principal-component analysis (PCA) showed that both hPSC lines cluster together and that the biggest variation (PC1) reflects the CM differentiation time points (Figure 2A). Indeed, the typical milestone genes expected to be up-/downregulated during differentiation at specific time points followed a similar trend in both lines (Figure S3C).

Despite the greatest number of DEGs occurring early in differentiation, pairwise comparisons between WT and *HSPG2*$^{+/-}$ cells showed minimal transcriptional changes in the cell lines up to day 20 of differentiation (Figure 2B and S3D). At the final day 30 maturation time point, where few time-point-induced DEGs are observed in either line (Figures S3A and S3B), perlecan haploinsufficiency caused the greatest number of genotype-induced DEGs (361 DEGs; Figures 2B and S3D). GO enrichment analysis of the genotype-induced DEGs at day 30 showed that day 30 WT hPSC-CMs had increased expression of genes associated with cardiac muscle cell differentiation, muscle contraction, and calcium signaling but decreased expression of membrane, phospholipid efflux, and metabolic processes (Table S1; Figure 2C). These changes are characteristic of a less mature phenotype in day 30 *HSPG2*$^{+/-}$ hPSC-CMs. Additionally, day 30 *HSPG2*$^{+/-}$ hPSC-CMs showed bidirectional differential expression of extracellular-associated genes, with ECM genes decreasing and genes present in the extracellular space increasing, indicating altered matrix composition (Table S1; Figure 2C).

By comparing expression of the genes highlighted by the GO-term analysis between hPSC-CMs (WT and *HSPG2*$^{+/-}$), fetal and adult human ventricular CMs/tissues, we found that WT-hPSCF-CMs expressed broadly higher (and closer to adult) levels of these CM-function-associated genes than perlecan-haploinsufficient CMs (Figure S3E). Unbiased PCA further showed that while, as expected, *in vivo* and *in vitro* samples are different, the day 30 WT hPSC-CMs cluster was closer to the *in vivo* samples on PC1 (Figure 2D).

To understand better what is behind the transcriptional differences observed between the parental and *HSPG2*$^{+/-}$ lines, gene set enrichment analysis (GSEA) was performed at both days 20 and 30 of differentiation (Figures 2E; Table S2). Interestingly, at day 20, we found that the *HSPG2*$^{+/-}$ CMs downregulated mitotic-linked GO terms and upregulated calcium- and muscle-related terms, while at day 30, these cells had decreased muscle terms and enriched metabolism-linked terms, suggesting that the *HSPG2*$^{+/-}$ cells may be attempting to compensate

**Figure 2. Transcriptomic analysis of perlecan-deficient (*HSPG2*$^{+/-}$) hPSC-CMs**

(A) PCA plot of WT and *HSPG2*$^{+/-}$ CM differentiation from bulk RNA sequencing outputs at each time point, with time point clusters at days 0 (red), 6 (pink), 10 (yellow), 15 (green), 20 (cyan), and 30 (blue).

(B) Volcano plot showing differentially expressed genes (DEGs) between each time point with positive (red) and negative (blue) log fold changes indicated and genes not meeting the thresholds in gray.

(C) Overrepresentation analysis of the 361 DEGs by genotype at day 30, assessed against the biological processes sets (GO consortium).

(D) PCA plot of WT hPSC-CMs, *HSPG2*$^{+/-}$ hPSC-CMs, fetal human ventricular tissue, and adult human ventricular CMs.

(E) Gene set enrichment analysis (GSEA) at days 20 and 30.

(F) *NNAT* and *PLN* gene counts following deSeq2 normalization of RNA sequencing analysis during hPSC-CM differentiation. Data, mean ± SD. Significance was determined by one-way ANOVA, $^{**}p < 0.01$, $^{***}p < 0.001$, $n = 3$.

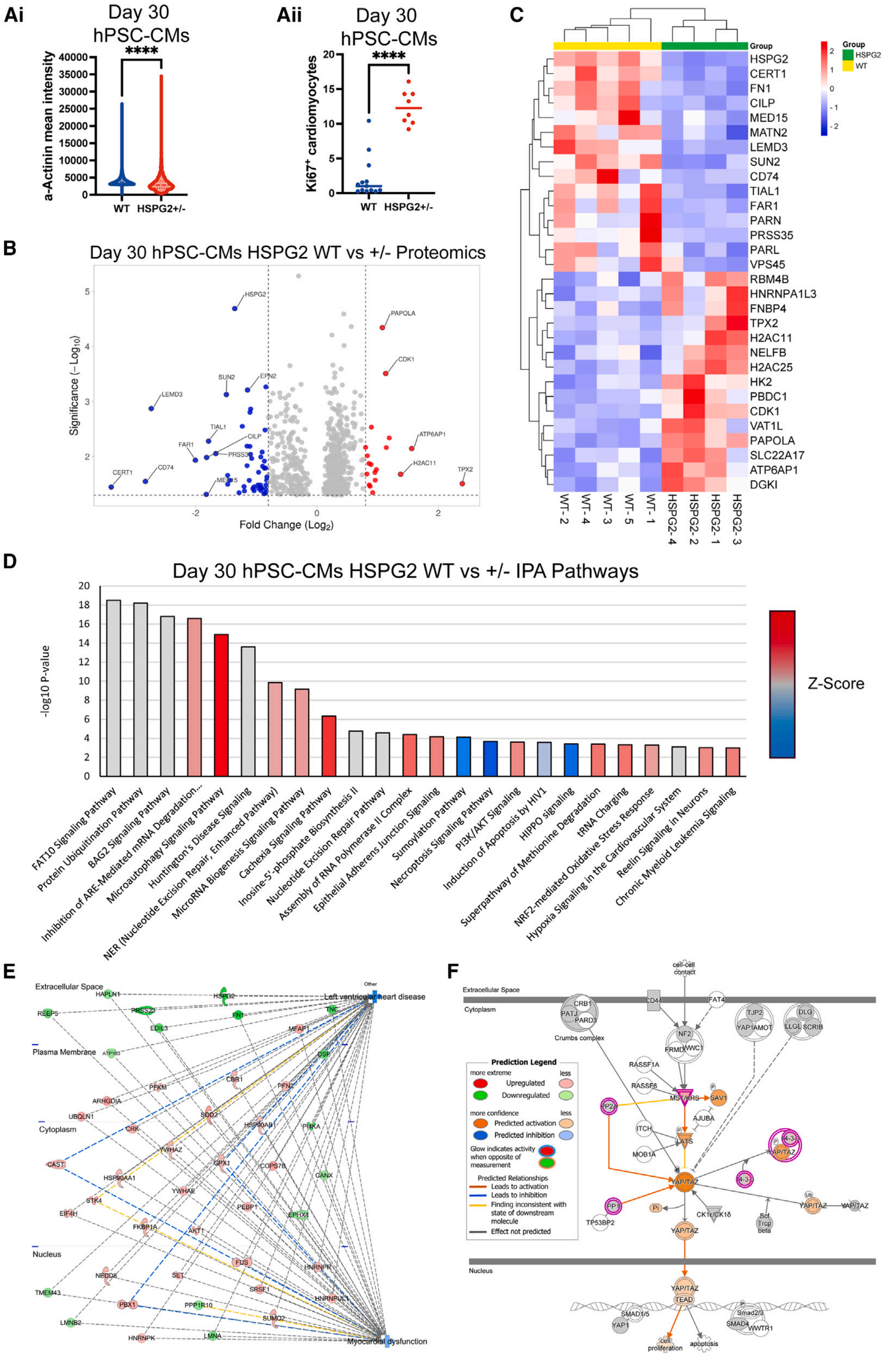

(legend on next page)

for an imbalance at day 20 but by day 30 are unable to keep up and succumb to structural and metabolic disfunction.

This result prompt us to determine what are the genotype-induced DEGs early in differentiation. We identified 11 common DEGs prior to maturation including, reassuringly, *HSPG2* (Figures S3F and S3G). Of these, 4 were higher in *HSPG2*$^{+/-}$ (*ZNF676*, *SVIL-AS1*, *MGMT*, and *TRIM61*), and 7 were higher in the parental line (*HSPG2*, *NNAT*, *SLC15A4*, *KCNC3*, *RBM46*, *GLT1D1*, and *TMSB4Y*) (Figure S3G). Transcript analysis showed *HSPG2*, *NNAT*, and ZNF676 to be the most abundant genes of the set (Figure S3H). *NNAT* (encoding neuronatin), in particular, a developmental gene associated with glucose metabolism and calcium signaling that shares 50% sequence homology with *PLN* (encoding phospholamban),[28,29] had the second highest gene count. Interestingly, *NNAT* expression was consistently low in *HSPG2*$^{+/-}$ cells, while *PLN* expression was only downregulated in day 30 *HSPG2*$^{+/-}$ hPSC-CMs when *NNAT* expression was no longer dysregulated (Figure 2F), highlighting that perlecan deficiency may lead to a calcium/metabolic imbalance in CMs prior to their development of a more severe phenotype.

In summary, perlecan deficiency induced transcriptional changes linked to contractility, metabolism, calcium signaling, and ECM remodeling during the maturation stage of hPSC-CM differentiation. These changes suggest that perlecan is required for CM maturation and that, while the mechanism of action is unclear, data point to a dysregulation of *NNAT* and *PLN* expression.

## Perlecan-deficient CMs express half the amount of perlecan and have dysregulated metabolism and increased proliferation

In keeping with a less mature phenotype, day 30 *HSPG2*$^{+/-}$ hPSC-CMs expressed lower levels of α-actinin (Figure 3Ai).[27] Thus, next we explored if at the protein level, these mutant cells also displayed dysfunctional maturity-linked pathways by running proteomic mass spectrometry on day 30 WT and *HSPG2*$^{+/-}$ hPSC-CM samples. As expected, perlecan expression levels in the mutant cells were half of those in the WT samples at day 30 (Figures 3B and 3C). We next used ingenuity pathway analysis (IPA) to determine how the mutant phenotype affected the CMs (Figure 3D). Various pathways were dysregulated in the mutant, including cell-cycle-progression- and mitochondrial-function-linked pathways (Figures S4A and S4B). Myocardial dysfunction and heart disease pathways were also dysregulated in day 30 *HSPG2*$^{+/-}$ hPSC-CMs, providing further evidence of the importance of perlecan in functional CM development (Figure 3E).

CM maturation is typically linked to a reduction in cell proliferation,[10] and in keeping with the thesis that normal perlecan levels are needed to promote CM maturation, we observed that day 30 *HSPG2*$^{+/-}$ hPSC-CMs proliferate more than day 30 WT hPSC-CMs as per Ki67$^{+}$ staining (Figure 3Aii). This may be linked to dysregulation in the HIPPO pathway in the mutant cells (Figure 3F).

All these results confirm that perlecan haploinsufficiency leads to the generation of CMs deficient in three hallmarks of maturity: α-actinin intensity, number of non-proliferative cells, and metabolism dysregulation.

## *HSPG2*$^{+/-}$ hPSC-CMs show reduced metabolic substrate capacity and an increased reliance on glycolytic metabolism

Since both RNA sequencing and proteomic mass spectrometry analysis suggested that perlecan haploinsufficiency affects metabolic pathways, next we assessed how the *HSPG2*$^{+/-}$ mutation impacted cellular metabolism. First, we performed mitochondria shape analysis based on TOMM20 staining in day 30 CMs. *HSPG2*$^{+/-}$ hPSC-CMs had increased mitochondria in the peri-nuclear area but less mitochondria in the cytoplasm (albeit a smaller but significant difference), and these were also less elongated (form factor) and less interconnected, i.e., mitochondria had less branching points (aspect ratio), suggesting that, overall, WT hPSC-CMs have more mature mitochondrial networks (Figures S5A and S5B).

Next, we assessed mitochondrial substrate capacity using a MitoPlate (Biolog) assay previously optimized to measure maximal metabolism across hPSC-CM differentiation (Figures 4A–4D).[30] Both *HSPG2*$^{+/-}$ and WT lines displayed the expected trend of increased metabolite usage capacity along the differentiation and up to day 20 (Figure S5C). However, early *HSPG2*$^{+/-}$ CMs (day 10) showed an increase in metabolite usage capacity (10 of the 16 substrates tested), followed by a reduction in capacity at day 30 in comparison to WT controls (Figures 4A–4D). Interestingly, the only 2 substrates unaffected at day 30 in *HSPG2*$^{+/-}$ CMs were both glycolytic substrates (α-D-glucose and glycogen), indicating that the capacity to metabolize these substrates was not reduced by perlecan deficiency.

To further interrogate functional metabolic differences, the Seahorse metabolic flux assay was performed on day 30 WT and *HSPG2*$^{+/-}$ hPSC-CMs. No major differences in oxygen consumption rate (OCR), a measure of mitochondrial respiration, were observed between the lines except for basal respiration in day 30 samples (Figures 4E and 4G). Quantification of these results confirmed basal, but not maximal, respiration, or the spare respiratory capacity of the cells was increased in day 30 mutant CMs (Figures 4G–4I). ATP linked to respiration and non-mitochondrial respiration was also increased in day 30 mutant CMs (Figures 4J and 4K). On the other hand, a striking difference between the lines was observed in extracellular

**Figure 3. Comparative analysis of day 30 WT and *HSPG2*$^{+/-}$ hPSC-CMs**

(A) High content image analysis quantification of (Ai) α-actinin mean intensity and (Aii) Ki67$^{+}$ CMs as determined by α-actinin staining. Significance was determined using t test, ****$p < 0.0001$, n = 3 with 2–3 technical wells per experiment, from which hundreds of cells were quantified.

(B and C) Label-free LC-MS/MS analysis showing DEPs as (B) volcano plot with positive (red) and negative (blue) log fold changes indicated and (C) heatmap of top 30 DEPs.

(D–F) Ingenuity pathway analysis of DEPs identified multiple (D) differential canonical pathways, with networks for (E) left ventricular heart disease-myocardial dysfunction and (F) HIPPO signaling pathway presented. Proteins in green are higher in WT hPSC-CMs, and proteins in red are higher in *HSPG2*$^{+/-}$ hPSC-CMs. Significance was determined by one-way ANOVA, ****$p < 0.0001$, n = 5.

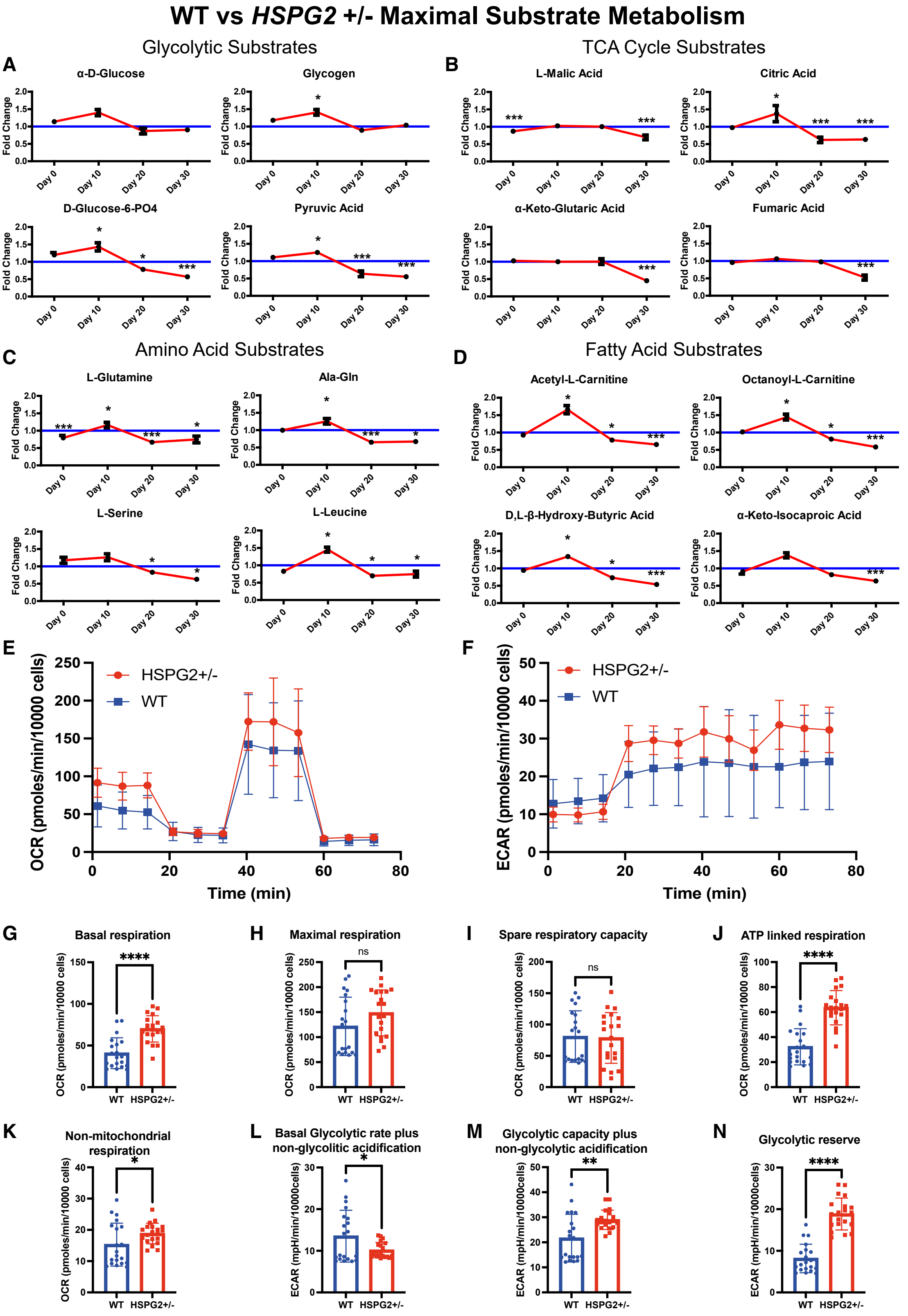

*(legend on next page)*

acidification rate (ECAR), a measure of glycolytic metabolism, which was significantly increased in *HSPG2*$^{+/-}$ hPSC-CMs upon oligomycin addition (Figure 4F). Quantification of these results showed that day 30 WT CMs had a lower glycolytic capacity and glycolytic reserve than *HSPG2*$^{+/-}$ hPSC-CMs, but the basal glycolytic rate was slightly elevated in WT versus *HSPG2*$^{+/-}$ hPSC-CMs (Figures 4L–4N). Overall, these data indicate that *HSPG2*$^{+/-}$ haploinsufficient cells have a higher reliance on glycolytic metabolism.

Together, this metabolic analysis showed that, while perlecan deficiency does not lead to lower respiration capacity in matured CMs, it promotes a greater reliance on glycolytic forms of metabolism, characteristic of hindered CM maturation. This is in keeping with the more immature mitochondrial architecture of perlecan-deficient CMs.

## *HSPG2*$^{+/-}$ engineered heart tissues are thinner and exhibit reduced contractile force production

To understand how perlecan deficiency impacted on contractile function, we encapsulated WT and *HSPG2*$^{+/-}$ hPSC-CMs into 3D engineered heart tissues (EHTs). EHTs have been shown to further enhance hPSC-CM maturation beyond the level seen in 2D cultures,[31,32] providing a model in which contractile force can be measured.[33] *HSPG2*$^{+/-}$ EHTs, while expressing similar levels of *ACTN2* (Figures S6A and S6B), had a 50% reduction in perlecan (Figures S6C and S6D) and likely a very different ECM composition since they displayed a significant reduction in tissue thickness (>50%) (Figure 5A).

Analysis of EHTs without electrical pacing showed no difference in spontaneous beat rate between WT and *HSPG2*$^{+/-}$ EHTs (Figure 5B). However, *HSPG2*$^{+/-}$ EHTs displayed a reduction in both contraction peak amplitude and relaxation time, but no changes were observed in contraction time (time to peak) or overall contraction/relaxation cycle (peak to peak) (Figures 5C–5F). Upon 0.5 Hz frequency stimulation, the results were similar, with *HSPG2*$^{+/-}$ EHTs showing significantly decreased force but no difference in contraction dynamics (Figures S4D–S4H).

This functional dysregulation could be a consequence of abnormal signaling during maturation. Given that in other contexts, e.g., in neurons or chondrocytes, perlecan has been shown to bind the DGC to mediate intracellular signaling,[19,34] we next determined if also in CMs can perlecan bind the DGC. Co-immunoprecipitation (IP) confirmed that perlecan binds to DGC, but no difference in binding was observed between WT and perlecan-haploinsufficient cells (Figures 5G and 5H). We did, however, note that less agrin was pulled down with DGC than with perlecan at days 6 and 20 (Figure 5I), but this is not a quantitative method, and therefore these data are only suggestive. Moreover, we found that the bond between the DGC and perlecan or agrin was so strong that these complexes could not be denatured post-IP, and consistently we identified, upon western blot, supercoiled aggregates of α-DGC plus smaller (or cleaved) forms of perlecan or agrin since, even when using a strong denaturing reagent (TCEP), α-DGC runs at the same level as the complexes (Figure 5J).

Together, these data demonstrate that *HSPG2*$^{+/-}$ mutation leads to reduced EHT thickness and contraction force, and importantly, we confirm that this functional dysregulation may be mediated via perlecan binding to the DGC.

## Maturation on synthetic PER-P-coated substrate enhanced multinucleation of hPSC-CMs

Given that perlecan haploinsufficiency compromised CM maturation functionally at multiple levels, we next cultured WT hPSC-CMs on a PER-P-coated substrate to investigate the effect of extra perlecan binding on CM maturation. Cells were exposed to PER-P for the final 10 days of maturation. At day 30, a striking difference in cell morphology was observed, with sarcomeric structures and borders between hPSC-CMs becoming less defined and an increase in the level of multinucleated hPSC-CMs observed in PER-P-coated dishes (Figure 6A). Although hPSC-CMs experience a degree of multinucleation during maturation on control dishes (vitronectin [VTN] coated), increased nucleation (>8), often in a circular profile, was seen on PER-P-coated dishes (Figure 6B). High content imaging (>30,000 cells per condition), previously developed to quantify nucleation in a hPSC-CM model of hypertrophy,[35] confirmed this result (Figure 6C). Specifically, mononucleated cells were the major hPSC-CM population in both lines but decreased from 90.1% ± 2.8% to 75.1% ± 1.5% on PER-P. Conversely, the proportions of binuclear and multinuclear populations increased on PER-P from 9.0% ± 2.3% to 18.8% ± 1.2% and from 0.9% ± 0.5% to 5.7% ± 0.5%, respectively.

Multinucleation is typically associated with hypertrophic growth; thus, we evaluated cell volume using flow cytometry as previously described.[36] As expected, cells grown on PER-P were significantly enlarged in comparison to cells grown in VTN (Figure 6D).

To investigate potential pathways involved in regulating these PER-P-induced morphological differences, real-time PCR was performed on candidate genes involved in sarcomeric structure, metabolism, ECM, and calcium signaling, the pathways known to be dysregulated in *HSPG2*$^{+/-}$ hPSC-CMs (Tables S1 and S2; Figures 2D, 2E, and 6E). While dysregulation was broadly seen in a number of these genes, the trend was not always the opposite of what we observed in the perlecan-haploinsufficient cells (Table S3). The profile of structural sarcomeric encoding genes was significantly altered, with troponin genes (*TNNI1* and *TNNI3*) decreased and myosin heavy chain genes (*MHY6* and *MHY7*) increased on the PER-P substrate. Cardiac actin (*ACTC1*) expression was, however, unaltered.

**Figure 4. Metabolic analysis of day 30 perlecan-deficient (*HSPG2*$^{+/-}$) hPSC-CMs**

(A–D) Maximum metabolic capacity of (A) glycolysis, (B) TCA cycle, (C) amino acid, and (D) fatty acid substrates, determined through Biolog MitoPlate assay. Data are presented as fold change of *HSPG2*$^{+/-}$ line compared to WT controls. Significance was determined using t test, $^{*}p < 0.05$, $^{**}p < 0.01$, $^{***}p < 0.001$, n = 3 with 3 technical repeats per experiment.

(E–N) Seahorse metabolic analysis of D30 WT and *HSPG2*$^{+/-}$ hPSC-CMs, showing (E) normalized oxygen consumption rate (OCR), (F) extracellular acidification rate (ECAR), and (G–N) quantification of metabolic readouts. Data, mean ± SD. Significance was determined using t test, $^{*}p < 0.05$, $^{**}p < 0.01$, $^{***}p < 0.001$, n = 2 with 10 technical repeats per experiment.

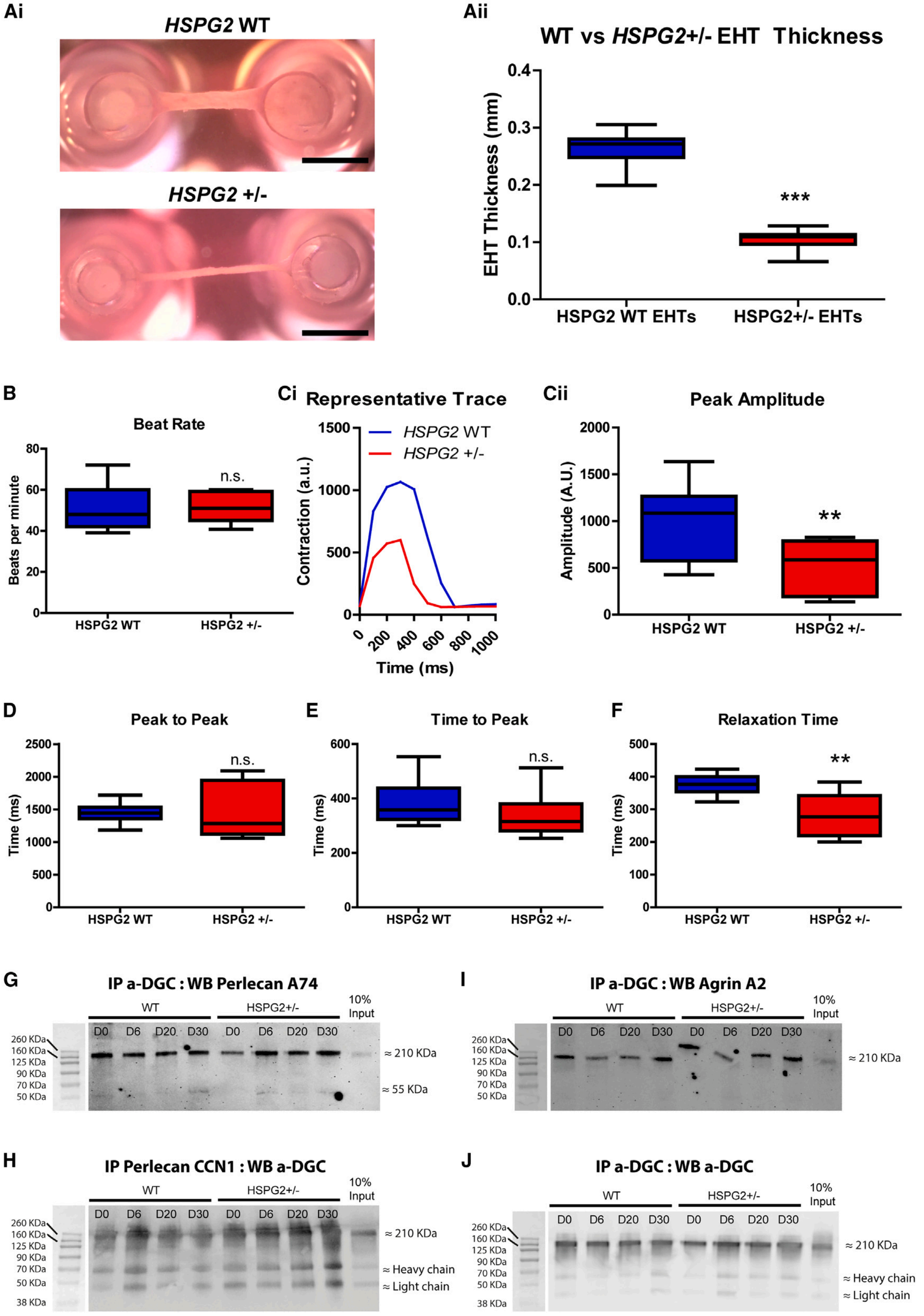

*(legend on next page)*

Metabolism-associated genes were also changed, with several glycolytic genes (*SLC2A1*, *SLC2A4*, *HK2*, and *LDHA*) and *ACYL*, a gene associated with fatty acid oxidation, increased. ECM-associated genes such as binding integrins were also altered, with integrin subunit α9 (*ITGA9*) increasing and *ITGB6* (associated with VTN binding) decreasing on PER-P. Lastly, the expression profile of several calcium signaling genes were also changed following PER-P maturation. Of note, *RYR2*, *PLN*, and *NNAT* expression increased, and the fold change of *NNAT* was particularly high, reflecting an opposite trend to that observed in the perlecan-haploinsufficient line.

Together, morphological and expression differences demonstrate that the PER-P substrate was capable of altering signaling during the maturation stage of CM differentiation. The morphological changes[37] and some of the expression changes (e.g., *MYH7* upregulation)[38] are characteristic of increased hypertrophic growth, confirming that perlecan plays a role in CM differentiation and phenotype.

## DISCUSSION

The role of perlecan in CM maturation was largely unknown. In chondroprogenitors and neurons, perlecan is known to play key signaling roles in ECM maturation and stabilisation.[34] Our results suggest that the same is true for its role in CMs. Namely, we show using a haploinsufficient hPSC line and a protocol that generates ventricular CMs with mature properties[27] that perlecan is essential for CM maturation and that it contributes to improved ECM synthesis, contraction, and metabolism. Complementary to this, we show that WT cells grown on a PER-P substrate develop hypertrophic features, thus leading us to propose that perlecan may be involved in the hypertrophic growth phase of CM maturation.

### Perlecan signaling during the maturation of hPSC-CM differentiation

hPSC-CM differentiation protocols are still limited in that they generate CMs with an immature, fetal-like nature,[39–41] despite the many maturation strategies that have been tested with various degrees of success.[42–54] Here, we explored the hypothesis that perlecan contributes to CM maturation. Surprisingly, we found that perlecan acts in an opposite manner to agrin, i.e., rather than promoting immature features and proliferation, it promoted multinucleation and other hypertrophic features.[2,14–16,55] The maturity features associated with perlecan in our cultures are corroborated by several studies, which implicate perlecan signaling, at least in part, in CM maturation induced through *in vivo* transplantation/prolonged culture,[56] co-culture interactions,[57] and direct interactions with ECM maturation substrates.[58]

A previous study has also reported the increasing expression of perlecan during hPSC-CM differentiation.[59] This led Robert et al.[59] to suggest perlecan as a candidate with potential to promote greater cardiomyogenic induction and/or CM maturation. Perlecan-deficient murine embryonic stem cells have also been reported, and these produced CMs with unaffected sarcomere formation and cellular functional properties, despite the parental heterozygous mice exhibiting reduced heart function.[25] This 2008 study used a basic CM differentiation protocol in which maturation was not promoted, potentially explaining the discrepancy between their *in vitro* and *in vivo* data. Both these studies support our findings, showing that perlecan expression peaks in late-stage hPSC-CM differentiation, with maturation required for its signaling effects to become evident.

### The role of perlecan in CM metabolic development

Here, we identified CM metabolism as significantly disrupted in perlecan-deficient cells at its transcriptomic, proteomic, and functional levels. Pre-maturation (day 0–15) perlecan deficiency downregulated *SLC15A4*, a gene encoding an amino acid and oligopeptide transporter, shown to be the gatekeeper of metabolic shifts in macrophage phenotypic switching.[60] On the other hand, *SLC2A1*, encoding for glucose transporter 1, was among the DEGs identified in late-stage perlecan-deficient CMs. Dysregulation of *SLC2A1* is of particular interest since neuronatin is an important protein for glucose transport, impacting whole-body metabolism through this gene.[29,61,62] Together, the transcription data suggested that perlecan deficiency leads to changes in glucose handling, and functional analysis confirmed that late-stage perlecan-deficient CMs have an increased reliance on glycolytic metabolism.

During normal CM differentiation, mitochondria maturation leads to hPSC-CMs switching from predominately glycolysis and glutamine oxidation metabolism to a higher reliance on lactate and fatty acid oxidative metabolism.[63] Here, we found that perlecan haploinsufficiency led to more immature mitochondrial networks and a higher number of peri-nuclear mitochondria. The increased glycolytic capacity of perlecan-deficient hPSC-CMs suggests that these cells have equally more immature metabolism. Whether the increased glycolytic reliance is a consequence of hindered development, or the cause of it, is an open question. Irrespective of this, it is evident that perlecan deficiency affects the typical metabolic maturation trajectory of CMs and their mitochondria network.

**Figure 5. Generation of *HSPG2*$^{+/-}$ engineered heart tissues (EHTs) and co-immunoprecipitation with α-DGC**

(Ai) Bright-field images of WT and *HSPG2*$^{+/-}$ EHTs, showing morphological changes after 14 days in culture (scale bar: 1 cm).

(Aii) Measurements of EHT thickness were performed by triple measurements along each EHT and averaged (WT n = 16, *HSPG2*$^{+/-}$ n = 11). Significance was determined by non-parametric t test, ***$p < 0.001$.

(B) Beat rate analysis.

(Ci) Representative traces of spontaneous contraction as determined using MUSCLEMOTION software.

(Cii–F) Quantification of contraction dynamics using MUSCLEMOTION software. Data, mean ± SD. Significance was determined by non-parametric t test, **$p < 0.01$, ***$p < 0.001$.

(G–J) Co-immunoprecipitation studies showing (G) α-DGC pulls down perlecan, (H) perlecan pulls down α-DGC, and (I) α-DGC pulls down agrin, and in (J) is a control showing the α-DGC western blot of α-DGC pull-down. Ladder is indicated on the left of the western blots, and estimated band size is indicated on the right.

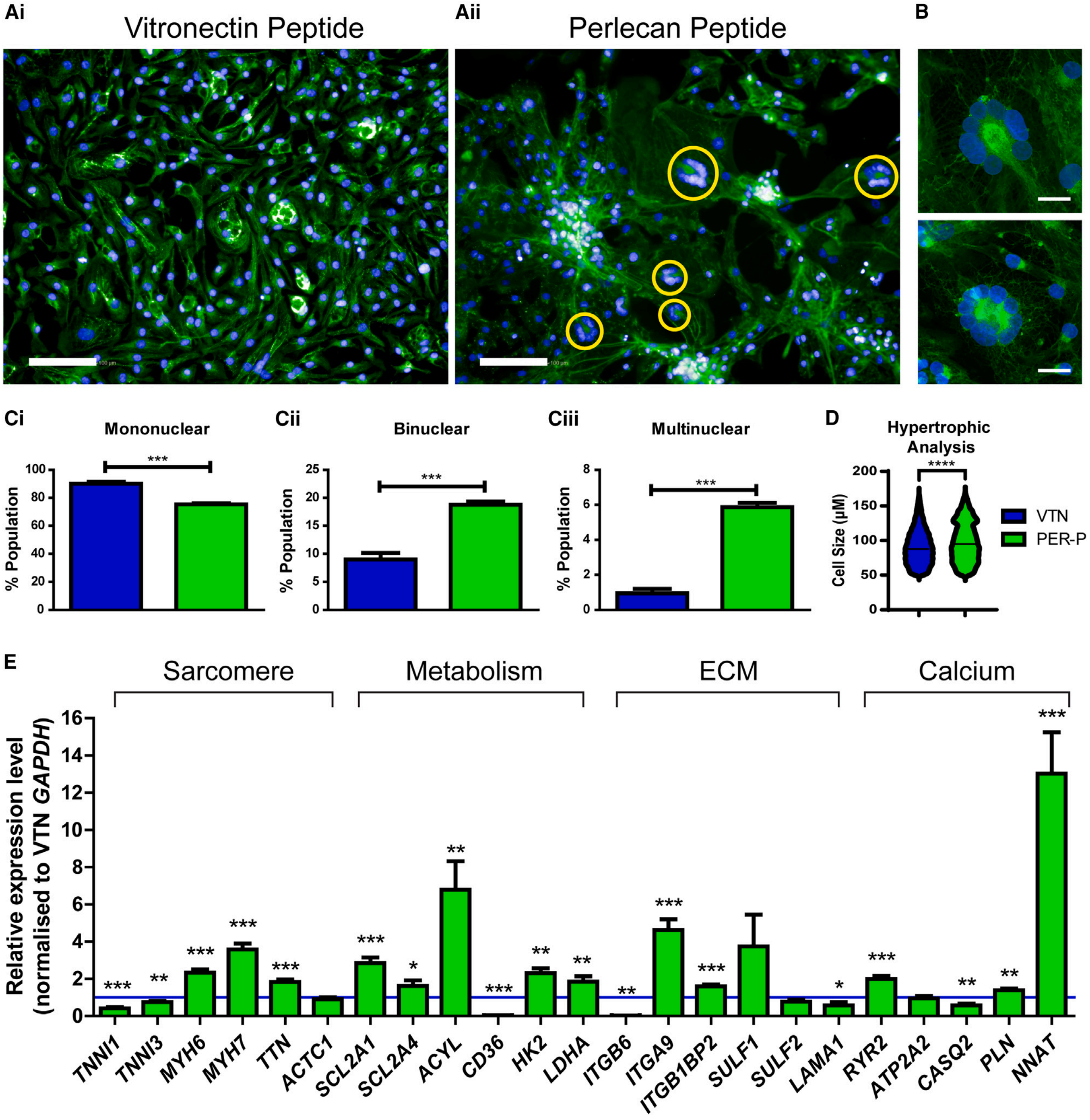

**Figure 6. Maturation of WT hPSC-CMs on a perlecan peptide (PER-P)-coated substrate**

(A and B) Day 30 hPSC-CMs grown from days 20 to 30 on either a PER-P-coated substrate or a vitronectin (VTN)-peptide-coated substrate were stained with α-actinin (green) and DAPI (blue).

(A) Fluorescent images showing morphology difference and highlighting presence of multinucleated populations (yellow rings) in cells grown on PER-P. Scale bar: 100 μm.

(B) High-resolution examples of multinuclear populations in the PER-P substrate. Scale bar: 20 μm.

(C) Quantification of nucleation at day 30 on each substrate using high content image analysis algorithm to distinguish between mono-, bi-, and multinucleation (>30,000 cells/condition).

(D) Flow cytometry quantification of hypertrophic cell size.

(E) SYBR Green real-time PCR analysis of structural sarcomeric, metabolic, ECM, and calcium signaling genes normalized to expression level on control VTN surfaces (n = 3). Data, mean ± SD. Significance was determined by multiple t tests, *p < 0.05, **p < 0.01, ***p < 0.001.

**Table 1. Primer sequences used for SYBR green real-time PCR**

| Gene primer | Forward sequence (5′-3′) | Reverse sequence (5′-3′) |
|---|---|---|
| *ACTC1* | CCAGCCCTCCTTCATTGGT | GGTGCCTCCAGATAAGACATTGTT |
| *ACYL* | GCTCTGCCTATGACAGCACCAT | GTCCGATGATGGTCACTCCCTT |
| *AGRN* | TCCTGCAAGGTTCGGGT | GTCCCGGGTTTATCTTC |
| *ATP2A2* | CGGAATTCATGCGCAGTGATAAATTGAC | CTCGGATCCAACACTACAGGTGTTGAATGG |
| *CASQ2* | AGCTTGTGGAGTTTGTGAAG | GGATTGTCAGTGTTGTCCC |
| *CD36* | AGCTTTCCAATGATTAGACG | GTTTCTACAAGCTCTGGTTC |
| *GAPDH* | GTCTCCTCTGACTTCAACAGCG | ACCACCCTGTTGCTGTAGCCAA |
| *HK2* | GTCCGATGATGGTCACTCCCTT | GTCCGATGATGGTCACTCCCTT |
| *HSPG2* | AGCATCTCAGGAGACGACCT | GAAATTCACCAGGGCTCGGA |
| *ITGA9* | GACGCTGATCCCTTGCTATGA | CGGTGAAGAAGCCCGCTATC |
| *ITGB1BP2* | GATGCACTTAAGGGTTGGTCCT | TGTAGCAGGGCCTTCAGGTT |
| *ITGB6* | GCAAGCTGCTGTGTGTAAGGAA | CTTGGGTTACAGCGAAGATCAA |
| *LAMA1* | GTTTCGAACCTCCTCGCAGA | CTTGCCGTCCACAAGCTCTAGT |
| *LDHA* | GTCCGATGATGGTCACTCCCTT | GTCCGATGATGGTCACTCCCTT |
| *MYH6* | CAACAATCCCTACGACTACGC | ACGTCAAAGGCACTATCGGTG |
| *MYH7* | CACTGATAACGCTTTTGATGTGC | TAGGCAGACTTGTCAGCCTCT |
| *NNAT* | CGGCTGGTACATCTTCCGC | TGTCCCTGGAGGATTTCGAAA |
| *PLN* | AGCACGTCAAAAGCTACAGAATCT | CTGATGTGGCAAGCTGCAGATC |
| *RYR2* | GTCCGATGATGGTCACTCCCTT | GTCCGATGATGGTCACTCCCTT |
| *SLC2A1* | CATCAACGCTGTCTTCTATTACTC | ATGCTCAGATAGGACATCCA |
| *SLC2A4* | CTTCGAGACAGCAGGGGTAC | ACAGTCATCAGGATGGCACA |
| *SULF1* | AGACCTAAGAATCTTGATGTTGGAA | CCATCCCATAACTGTCCTCTG |
| *SULF2* | GACCCCTACCAGCTGATGAA | GCTTGTAACCCTTGCAGCTC |
| *TNNI1* | GCAGCGCCTGCATCATG | AGTCACCAAGAACATCACGGAGAT |
| *TNNI3* | CGTGTGGACAAGGTGGATGA | TTCCTTCTCGGTGTCCTCCT |
| *TTN* | GGAAGAAGTTGTTCTGAAAAGCG | GTTTTGGAGGTGGTGGTTCTG |

### The role of perlecan in ECM remodeling and cardiac contractility

Perlecan has been identified as the key regulatory hub in the maintenance and turnover of basement membrane ECM.[64] Moreover, perlecan knockdown has previously been associated with global changes to ECM development in a cartilage model of Schwartz-Jampel syndrome (SJS) and with immature ECM formation in aortic tissue.[65,66] Our findings suggest that CM development is similarly impacted upon perlecan deficiency, i.e., we saw that perlecan deficiency leads to both ECM-related gene transcriptomic changes and to functional changes likely linked to ECM alterations. Specifically, perlecan-deficient EHTs formed significantly thinner tissues that generated reduced contractile force. This resembled the changes typically seen in EHTs with high levels of fibroblast incorporation, which are also thinner and generate less contraction force and where fibroblasts function as a key ECM remodeling cell type.[67] These similarities suggest that perlecan may also play a role in CM ECM remodeling. Experiments where WT CMs were grown on a synthetic PER-P surface further substantiate this conclusion since these hPSC-CMs exhibited altered expression of ECM and structural genes.

Cardiac ECM remodeling during postnatal growth increases myocardial stiffness, promoting CM cell-cycle arrest and maturation.[16,68,69] Thus, the ECM changes we see in perlecan-deficient EHTs, and their subsequent mechanical decline, could indicate that perlecan accumulation during CM differentiation contributes to mechanical remodeling and increased stiffness, creating an environment more permissive of maturation. It is unclear, however, if the contraction force reduction seen in perlecan-deficient EHTs is a direct result of increased tissue remodeling. Instead, it could also reflect calcium signaling dysregulation within perlecan-deficient CMs, as highlighted by the transcriptomic analysis. Indeed, previous studies have implicated perlecan in calcium signaling.[70]

*NNAT* and *PLN*, two prominent and related calcium-linked genes were dysregulated in both perlecan-deficient CMs and in WT hPSC-CMs grown on a PER-P substrate.[28,29,71–73] More investigation is, however, required to determine if *NNAT* and/or *PLN* play(s) a direct role in the development of CMs and to validate them as direct downstream targets of perlecan.

### The role of perlecan in CM proliferation, multinucleation, and hypertrophy

Cell-cycle activity in postnatal CMs usually results in polyploid cells with multiple nuclei, in what is known as the hypertrophic growth phase of CM development.[37,74,75] However, increased CM ploidy is not only linked to normal physiological development but also to disease environments such as hypertrophy.[37,76–78]

Here, we report a direct relationship between perlecan signaling, proliferation, multinucleation, and hypertrophy, suggestive of its involvement in CM hypertrophic development and/or pathology. Specifically, we demonstrate that while perlecan haploinsufficiency promotes increased proliferation, growing hPSC-CMs on a PER-P-coated substrate produced enlarged CMs with increased multinucleation. Although this enhanced multinucleation is possibly due to enhanced maturity, the gene expression profile does not support this and instead suggests that increased nucleation in this condition may be more representative of a pathological environment akin to pathological hypertrophy.[79] Perlecan has previously been implicated in hypertrophic signaling within CMs[80] as well as in non-cardiac tissues, including in chondrocytes[65] and skeletal muscle cells.[81] Our work shows, however, a direct causal effect between perlecan expression, proliferation/multinucleation, and hypertrophy, with the proteomic results further suggesting this may be due to perlecan-induced changes in the HIPPO pathway.

How perlecan mediates these and other functional changes is yet to be discovered, but here we confirm that also in CMs, perlecan binds the DGC, forming a tight protein complex, which in other contexts has been implicated in regulating intracellular signaling.[19,34] This complex was so tightly bound that it could not be separated with any reducing agent we tried (including TCEP), which is typical of protein complexes within the basement membrane.[82] Future work should further confirm if this interaction mediates perlecan signaling and how.

### Conclusions and future prospective

Here, we demonstrate that perlecan plays a role in CM maturation signaling, possibly through promoting mechanical (regulating matrix stiffness) or metabolic (regulating lipoprotein uptake) changes. Perlecan may also have a direct role in modulating growth factor signaling during maturation, as it is known to interact with many growth factors.[83] Gaining greater insights into the signaling roles of specific perlecan forms may lead to future maturation strategies, capable of exploiting these signaling roles. This approach could improve hPSC-CM cell quality for drug discovery pipelines, drug toxicity screening, and disease modeling applications.

Fetal phenotypic switch is common in many forms of heart failure, so future work may also aim to directly target perlecan to promote enhanced CM functionality in patients with heart failure. Given that our data implicate perlecan in CM hypertrophic growth and maturation, exploiting perlecan signaling to reverse this switch may be a promising strategy in many disease settings. Of note, targeting perlecan signaling has recently become a promising strategy in pancreatic cancer,[84] and as such, therapies in development may have potential for repurposing.

### Limitations of the study

Heterozygous knockouts are commonly used to manipulate gene dosage in functional studies, with findings complimented with further reduction through homozygous knockouts. The lack of a homozygous *HSPG2*$^{-/-}$ hPSC line is a limitation of our study. We tried to generate such lines but were unable to stabilize a line in culture. This may reflect the fact that fibroblast growth factor (FGF) signaling is required for hPSC maintenance[85–87] and that FGF signaling is facilitated through its binding to perlecan,[88–90] including in the context of stem cell self-renewal.[91] Thus, we believe that FGF signaling impairment prevented the generation of *HSPG2*$^{-/-}$ hPSC lines in this study and propose that in the future, a conditional knockout is made to circumvent this problem.

Analysis of hPSC-CM models must account for their limitations, namely their typical immature status. As such, advanced systems are required to produce the most appropriate model systems. Here, we utilized a differentiation protocol capable of enhanced maturity and 3D tissue systems that could further promote maturation.[27] The maturation of these tissue could be further enhanced through *in vivo* transplantation[54] or via mechanical pacing and stretching.[92] Although we did not investigate either in this study, the effect of *in vivo* hPSC-CM maturation on perlecan expression has been described; Yokoyama et al. showed that 12 week *in vivo* maturation of 3D hPSC-CM tissue induced prominent perlecan protein expression,[56] further supporting the conclusions of our work. Additionally, to overcome the maturity limitations of hPSC-CMs, it would have been interesting to compare the *in vitro* hPSC-CM findings with what is observed in primary CMs from a *HSPG*$^{+/-}$ mouse model.

Our findings suggest that perlecan may have value as a substrate for hPSC-CM *in vitro* maturation. A limitation of our work is that the synthetic PER-P substrate investigated promoted nucleation and hypertrophy more representative of a pathological environment rather than developmental maturation. Although this PER-P did not enhance hPSC-CM maturation, it is interesting to note that a commercial hPSC-CM maturation substrate (Matrix Plus) comprises high perlecan content. This biological hPSC-CM maturation substrate first reported by Block et al. has an increased abundance of perlecan (from 7.4% to 19.7%), noted as a major difference compared to a non-maturing control ECM.[58] We suggest that, with further optimization of the PER-P form, concentration, and appropriate glycosaminoglycan incorporation, a synthetic perlecan surface that promotes hypertrophic growth more representative of advanced maturity can be obtained.

## STAR★METHODS

Detailed methods are provided in the online version of this paper and include the following:

- KEY RESOURCES TABLE
- RESOURCE AVAILABILITY
  - ○ Lead contact
  - ○ Materials availability
  - ○ Data and code availability
- EXPERIMENTAL MODEL AND STUDY PARTICIPANT DETAILS
  - ○ Ethics statement
  - ○ hPSC lines origin, characterization and maintenance
  - ○ Mouse embryo collections
  - ○ Human tissues
- METHOD DETAILS
  - ○ Cardiomyocyte differentiation from hPSCs and generation of 3D engineered heart tissue (EHT)
  - ○ Cardiomyocyte dissociation and replating
  - ○ Gene expression (real-time PCR)

  - ○ Gene expression (bulk RNA-sequencing)
  - ○ Differential expression and further data exploration
  - ○ Gene set enrichment analysis
  - ○ Gene expression heatmaps
  - ○ Differential transcript analysis
  - ○ Comparison to existing hPSC-CM bulk RNA-sequencing data
  - ○ Comparison to existing human tissues bulk RNA-sequencing data
  - ○ Protein analysis
  - ○ Immunostainng for high content imaging using Opera Phenix
  - ○ OPERA phenix imaging and harmony analysis
  - ○ Western blotting
  - ○ Label-Free liquid chromatography–tandem mass spectrometry (LC-MS/MS) analysis
  - ○ LC-MS/MS spectral acquisition
  - ○ Peptide identification and quantification
  - ○ Label-free quantification
  - ○ Statistical testing
  - ○ Ingenuity pathway analysis (IPA)
  - ○ Co-Immunoprecipitation
  - ○ Metabolic analysis
  - ○ Mitochondrial substrate BioLog assay
  - ○ Image acquisition
- QUANTIFICATION AND STATISTICAL ANALYSIS
  - ○ Image quantification
  - ○ Statistical analysis

## SUPPLEMENTAL INFORMATION

Supplemental information can be found online at https://doi.org/10.1016/j.celrep.2023.113668.

## ACKNOWLEDGMENTS

We would like to thank the Francis Crick Institute Making Lab scientific platform, especially Xavier Cano Ferrer and George Konstantinou, for support establishing the EHT imaging. We would also like to thank the following members of the Bernardo lab: Dr. Elisa Ferraro for help acquiring the EHT videos and Dr. Rebecca Hulbert and Dr. Victor Velecela for help with cells. We thank members of the advanced sequencing facility at the Francis Crick Institute for their expertise, support, and use of the facilities. We thank members of the Tedesco lab for advice and reagent sharing for western blot and Dr. Svend Kjaer and Sir Jim Smith for advice on coIPs. We thank Dr. James Turner and his lab at the Francis Crick for advice and support. Work in the A.S.B. lab was supported by a Wellcome Trust career re-entry fellowship (210987/Z/18/Z), an idea to innovation grant from the Francis Crick Institute (supported by MR/X50287X/1), and a LifeArc grant (LifeArc/Crick Translation Fund). L.I.T. was supported under the Wellcome Trust fellowship (210987/Z/18/Z). J.W. was supported by a Visiting Professorship from the Leverhulme Trust (VP1-2016-041). K.H. was supported by the UKRI BBSRC Norwich research park Bioscience doctoral training program (BB/T008717/1). C.D. was supported by British Heart Foundation (CRMR/21/290009 and PG/21/10545). We would also like to thank the School of Life Sciences Imaging Facility (SLIM) for support operating the Zeiss Celldiscoverer microscope (University of Nottingham). J.G.W.S. was supported by the Academy of Medical Sciences, the Wellcome Trust, the Government Department of Business, Energy and Industrial Strategy, the British Heart Foundation, and a Diabetes UK Springboard Award (SBF005\1057). J.G.W.S., C.D., M.J.P., T.L.H., and A.C. were supported by the British Heart Foundation (SP/F/22/150044).

## AUTHOR CONTRIBUTIONS

Conceptualization, J.G.W.S., A.S.B., C.L.R.M., and J.W.; methodology, J.G.W.S., A.S.B., B.B.J., T.G., L.T., S.A.R., M.J.P., and M.-V.C.; investigation, J.G.W.S., B.B.J., M.-V.C., L.I.T., T.L.H., T.G., K.H., O.-R.S., N.T.N.V., A.N., A.C., M.J.P.; formal analysis, J.G.W.S., B.B.J., A.S.B., M.-V.C., L.I.T., T.L.H, T.G., A.C., O.-R.S., and M.J.P.; manuscript writing and editing, J.G.W.S., B.B.J., A.S.B., C.D., C.L.R.M., J.W., L.T., and S.A.R.; funding acquisition, J.G.W.S., A.S.B., C.L.R.M., and J.W.; resources, J.W.; project supervision, J.G.W.S., A.S.B., C.D., C.L.R.M., J.W., L.T., and S.A.R.

## DECLARATION OF INTERESTS

A patent application related to the left ventricle CM differentiation protocol used in this work has been submitted (WO 2020/245612) and is partly licensed to Axol Biosciences. A.S.B. is a beneficiary of this license.

Received: May 22, 2023
Revised: November 1, 2023
Accepted: December 22, 2023

## REFERENCES

1. Guo, Y., and Pu, W.T. (2020). Cardiomyocyte Maturation: New Phase in Development. Circ. Res. *126*, 1086–1106.
2. Porrello, E.R., Mahmoud, A.I., Simpson, E., Hill, J.A., Richardson, J.A., Olson, E.N., and Sadek, H.A. (2011). Transient regenerative potential of the neonatal mouse heart. Science *331*, 1078–1080.
3. Laflamme, M.A., and Murry, C.E. (2011). Heart regeneration. Nature *473*, 326–335.
4. Engel, F.B., Schebesta, M., and Keating, M.T. (2006). Anillin localization defect in cardiomyocyte binucleation. J. Mol. Cell. Cardiol. *41*, 601–612.
5. Olivetti, G., Cigola, E., Maestri, R., Corradi, D., Lagrasta, C., Gambert, S.R., and Anversa, P. (1996). Aging, cardiac hypertrophy and ischemic cardiomyopathy do not affect the proportion of mononucleated and multinucleated myocytes in the human heart. J. Mol. Cell. Cardiol. *28*, 1463–1477.
6. Ali, S.R., Hippenmeyer, S., Saadat, L.V., Luo, L., Weissman, I.L., and Ardehali, R. (2014). Existing cardiomyocytes generate cardiomyocytes at a low rate after birth in mice. Proc. Natl. Acad. Sci. USA *111*, 8850–8855.
7. Jopling, C., Sleep, E., Raya, M., Martí, M., Raya, A., and Izpisúa Belmonte, J.C. (2010). Zebrafish heart regeneration occurs by cardiomyocyte dedifferentiation and proliferation. Nature *464*, 606–609.
8. Kikuchi, K., Holdway, J.E., Werdich, A.A., Anderson, R.M., Fang, Y., Egnaczyk, G.F., Evans, T., Macrae, C.A., Stainier, D.Y.R., and Poss, K.D. (2010). Primary contribution to zebrafish heart regeneration by gata4(+) cardiomyocytes. Nature *464*, 601–605.
9. Schnabel, K., Wu, C.C., Kurth, T., and Weidinger, G. (2011). Regeneration of cryoinjury induced necrotic heart lesions in zebrafish is associated with epicardial activation and cardiomyocyte proliferation. PLoS One *6*, e18503.
10. Hashmi, S., and Ahmad, H.R. (2019). Molecular switch model for cardiomyocyte proliferation. Cell Regen. *8*, 12–20.
11. Chute, M., Aujla, P., Jana, S., and Kassiri, Z. (2019). The Non-Fibrillar Side of Fibrosis: Contribution of the Basement Membrane, Proteoglycans, and Glycoproteins to Myocardial Fibrosis. J. Cardiovasc. Dev. Dis. *6*, 35.
12. Valiente-Alandi, I., Schafer, A.E., and Blaxall, B.C. (2016). Extracellular matrix-mediated cellular communication in the heart. J. Mol. Cell. Cardiol. *91*, 228–237.
13. Silva, A.C., Pereira, C., Fonseca, A.C.R.G., Pinto-do-Ó, P., and Nascimento, D.S. (2020). Bearing My Heart: The Role of Extracellular Matrix

on Cardiac Development, Homeostasis, and Injury Response. Front. Cell Dev. Biol. *8*, 621644.

14. Bassat, E., Mutlak, Y.E., Genzelinakh, A., Shadrin, I.Y., Baruch Umansky, K., Yifa, O., Kain, D., Rajchman, D., Leach, J., Riabov Bassat, D., et al. (2017). The extracellular matrix protein agrin promotes heart regeneration in mice. Nature *547*, 179–184.
15. Dempsey, C.E., Bigotti, M.G., Adams, J.C., and Brancaccio, A. (2019). Analysis of alpha-Dystroglycan/LG Domain Binding Modes: Investigating Protein Motifs That Regulate the Affinity of Isolated LG Domains. Front. Mol. Biosci. *6*, 18.
16. Notari, M., Ventura-Rubio, A., Bedford-Guaus, S.J., Jorba, I., Mulero, L., Navajas, D., Martí, M., and Raya, Á. (2018). The local microenvironment limits the regenerative potential of the mouse neonatal heart. Sci. Adv. *4*, eaao5553.
17. Bigotti, M.G., Skeffington, K.L., Jones, F.P., Caputo, M., and Brancaccio, A. (2020). Agrin-Mediated Cardiac Regeneration: Some Open Questions. Front. Bioeng. Biotechnol. *8*, 594.
18. McCarthy, K.J. (2015). The Basement Membrane Proteoglycans Perlecan and Agrin: Something Old, Something New. Curr. Top. Membr. *76*, 255–303.
19. Peng, H.B., Ali, A.A., Daggett, D.F., Rauvala, H., Hassell, J.R., and Smalheiser, N.R. (1998). The relationship between perlecan and dystroglycan and its implication in the formation of the neuromuscular junction. Cell Adhes. Commun. *5*, 475–489.
20. Sciandra, F., Bozzi, M., Bigotti, M.G., and Brancaccio, A. (2013). The multiple affinities of alpha-dystroglycan. Curr. Protein Pept. Sci. *14*, 626–634.
21. Costell, M., Carmona, R., Gustafsson, E., González-Iriarte, M., Fässler, R., and Muñoz-Chápuli, R. (2002). Hyperplastic conotruncal endocardial cushions and transposition of great arteries in perlecan-null mice. Circ. Res. *91*, 158–164.
22. Roediger, M., Kruegel, J., Miosge, N., and Gersdorff, N. (2009). Tissue distribution of perlecan domains III and V during embryonic and fetal human development. Histol. Histopathol. *24*, 859–868.
23. Costell, M., Gustafsson, E., Aszódi, A., Mörgelin, M., Bloch, W., Hunziker, E., Addicks, K., Timpl, R., and Fässler, R. (1999). Perlecan maintains the integrity of cartilage and some basement membranes. J. Cell Biol. *147*, 1109–1122.
24. Arikawa-Hirasawa, E., Wilcox, W.R., and Yamada, Y. (2001). Dyssegmental dysplasia, Silverman-Handmaker type: unexpected role of perlecan in cartilage development. Am. J. Med. Genet. *106*, 254–257.
25. Sasse, P., Malan, D., Fleischmann, M., Roell, W., Gustafsson, E., Bostani, T., Fan, Y., Kolbe, T., Breitbach, M., Addicks, K., et al. (2008). Perlecan is critical for heart stability. Cardiovasc. Res. *80*, 435–444.
26. Nakahama, M., Murakami, T., Kusachi, S., Naito, I., Takeda, K., Ohnishi, H., Komatsubara, I., Oka, T., Ninomiya, Y., and Tsuji, T. (2000). Expression of perlecan proteoglycan in the infarct zone of mouse myocardial infarction. J. Mol. Cell. Cardiol. *32*, 1087–1100.
27. Dark, N., Cosson, M.V., Tsansizi, L.I., Owen, T.J., Ferraro, E., Francis, A.J., Tsai, S., Bouissou, C., Weston, A., Collinson, L., et al. (2023). Generation of left ventricle-like cardiomyocytes with improved structural, functional, and metabolic maturity from human pluripotent stem cells. Cell Rep. Methods *3*, 100456.
28. MacLennan, D.H., and Kranias, E.G. (2003). Phospholamban: a crucial regulator of cardiac contractility. Nat. Rev. Mol. Cell Biol. *4*, 566–577.
29. Braun, J.L., Geromella, M.S., Hamstra, S.I., and Fajardo, V.A. (2020). Neuronatin regulates whole-body metabolism: is thermogenesis involved? FASEB Bioadv. *2*, 579–586.
30. Johnson, B.B., Reinhold, J., Holmes, T.L., Moore, J.A., Cowell, V., Bernardo, A.S., Rushworth, S.A., Vassiliou, V., and Smith, J.G.W. (2021). Modelling Metabolic Shifts during Cardiomyocyte Differentiation, Iron Deficiency and Transferrin Rescue Using Human Pluripotent Stem Cells. Metabolites *12*, 9.
31. Silbernagel, N., Körner, A., Balitzki, J., Jaggy, M., Bertels, S., Richter, B., Hippler, M., Hellwig, A., Hecker, M., Bastmeyer, M., and Ullrich, N.D. (2020). Shaping the heart: Structural and functional maturation of iPSC-cardiomyocytes in 3D-micro-scaffolds. Biomaterials *227*, 119551.
32. Branco, M.A., Cotovio, J.P., Rodrigues, C.A.V., Vaz, S.H., Fernandes, T.G., Moreira, L.M., Cabral, J.M.S., and Diogo, M.M. (2019). Transcriptomic analysis of 3D Cardiac Differentiation of Human Induced Pluripotent Stem Cells Reveals Faster Cardiomyocyte Maturation Compared to 2D Culture. Sci. Rep. *9*, 9229.
33. Mannhardt, I., Breckwoldt, K., Letuffe-Brenière, D., Schaaf, S., Schulz, H., Neuber, C., Benzin, A., Werner, T., Eder, A., Schulze, T., et al. (2016). Human Engineered Heart Tissue: Analysis of Contractile Force. Stem Cell Rep. *7*, 29–42.
34. Hayes, A.J., Farrugia, B.L., Biose, I.J., Bix, G.J., and Melrose, J. (2022). Perlecan, A Multi-Functional, Cell-Instructive, Matrix-Stabilizing Proteoglycan With Roles in Tissue Development Has Relevance to Connective Tissue Repair and Regeneration. Front. Cell Dev. Biol. *10*, 856261.
35. Mosqueira, D., Mannhardt, I., Bhagwan, J.R., Lis-Slimak, K., Katili, P., Scott, E., Hassan, M., Prondzynski, M., Harmer, S.C., Tinker, A., et al. (2018). CRISPR/Cas9 editing in human pluripotent stem cell-cardiomyocytes highlights arrhythmias, hypocontractility, and energy depletion as potential therapeutic targets for hypertrophic cardiomyopathy. Eur. Heart J. *39*, 3879–3892.
36. Mosqueira, D., Lis-Slimak, K., and Denning, C. (2019). High-Throughput Phenotyping Toolkit for Characterizing Cellular Models of Hypertrophic Cardiomyopathy In Vitro. Methods Protoc. *2*, 83.
37. Derks, W., and Bergmann, O. (2020). Polyploidy in Cardiomyocytes: Roadblock to Heart Regeneration? Circ. Res. *126*, 552–565.
38. Vigil-Garcia, M., Demkes, C.J., Eding, J.E.C., Versteeg, D., de Ruiter, H., Perini, I., Kooijman, L., Gladka, M.M., Asselbergs, F.W., Vink, A., et al. (2021). Gene expression profiling of hypertrophic cardiomyocytes identifies new players in pathological remodelling. Cardiovasc. Res. *117*, 1532–1545.
39. Denning, C., Borgdorff, V., Crutchley, J., Firth, K.S.A., George, V., Kalra, S., Kondrashov, A., Hoang, M.D., Mosqueira, D., Patel, A., et al. (2016). Cardiomyocytes from human pluripotent stem cells: From laboratory curiosity to industrial biomedical platform. Biochim. Biophys. Acta *1863*, 1728–1748.
40. Koivumäki, J.T., Naumenko, N., Tuomainen, T., Takalo, J., Oksanen, M., Puttonen, K.A., Lehtonen, Š., Kuusisto, J., Laakso, M., Koistinaho, J., and Tavi, P. (2018). Structural Immaturity of Human iPSC-Derived Cardiomyocytes: In Silico Investigation of Effects on Function and Disease Modeling. Front. Physiol. *9*, 80.
41. Karbassi, E., Fenix, A., Marchiano, S., Muraoka, N., Nakamura, K., Yang, X., and Murry, C.E. (2020). Cardiomyocyte maturation: advances in knowledge and implications for regenerative medicine. Nat. Rev. Cardiol. *17*, 341–359.
42. Ahmed, R.E., Anzai, T., Chanthra, N., and Uosaki, H. (2020). A Brief Review of Current Maturation Methods for Human Induced Pluripotent Stem Cells-Derived Cardiomyocytes. Front. Cell Dev. Biol. *8*, 178.
43. Kamakura, T., Makiyama, T., Sasaki, K., Yoshida, Y., Wuriyanghai, Y., Chen, J., Hattori, T., Ohno, S., Kita, T., Horie, M., et al. (2013). Ultrastructural maturation of human-induced pluripotent stem cell-derived cardiomyocytes in a long-term culture. Circ. J. *77*, 1307–1314.
44. Yang, X., Rodriguez, M., Pabon, L., Fischer, K.A., Reinecke, H., Regnier, M., Sniadecki, N.J., Ruohola-Baker, H., and Murry, C.E. (2014). Tri-iodo-l-thyronine promotes the maturation of human cardiomyocytes-derived from induced pluripotent stem cells. J. Mol. Cell. Cardiol. *72*, 296–304.
45. Correia, C., Koshkin, A., Duarte, P., Hu, D., Teixeira, A., Domian, I., Serra, M., and Alves, P.M. (2017). Distinct carbon sources affect structural and functional maturation of cardiomyocytes derived from human pluripotent stem cells. Sci. Rep. *7*, 8590.

46. Ribeiro, A.J.S., Ang, Y.S., Fu, J.D., Rivas, R.N., Mohamed, T.M.A., Higgs, G.C., Srivastava, D., and Pruitt, B.L. (2015). Contractility of single cardiomyocytes differentiated from pluripotent stem cells depends on physiological shape and substrate stiffness. Proc. Natl. Acad. Sci. USA *112*, 12705–12710.
47. Kroll, K., Chabria, M., Wang, K., Häusermann, F., Schuler, F., and Polonchuk, L. (2017). Electro-mechanical conditioning of human iPSC-derived cardiomyocytes for translational research. Prog. Biophys. Mol. Biol. *130*, 212–222.
48. Huethorst, E., Hortigon, M., Zamora-Rodriguez, V., Reynolds, P.M., Burton, F., Smith, G., and Gadegaard, N. (2016). Enhanced Human-Induced Pluripotent Stem Cell Derived Cardiomyocyte Maturation Using a Dual Microgradient Substrate. ACS Biomater. Sci. Eng. *2*, 2231–2239.
49. Lemoine, M.D., Mannhardt, I., Breckwoldt, K., Prondzynski, M., Flenner, F., Ulmer, B., Hirt, M.N., Neuber, C., Horváth, A., Kloth, B., et al. (2017). Human iPSC-derived cardiomyocytes cultured in 3D engineered heart tissue show physiological upstroke velocity and sodium current density. Sci. Rep. *7*, 5464.
50. Ulmer, B.M., Stoehr, A., Schulze, M.L., Patel, S., Gucek, M., Mannhardt, I., Funcke, S., Murphy, E., Eschenhagen, T., and Hansen, A. (2018). Contractile Work Contributes to Maturation of Energy Metabolism in hiPSC-Derived Cardiomyocytes. Stem Cell Rep. *10*, 834–847.
51. Beauchamp, P., Jackson, C.B., Ozhathil, L.C., Agarkova, I., Galindo, C.L., Sawyer, D.B., Suter, T.M., and Zuppinger, C. (2020). 3D Co-culture of hiPSC-Derived Cardiomyocytes With Cardiac Fibroblasts Improves Tissue-Like Features of Cardiac Spheroids. Front. Mol. Biosci. *7*, 14.
52. Burnham, M.P., Harvey, R., Sargeant, R., Fertig, N., and Haddrick, M. (2021). A Scalable Approach Reveals Functional Responses of iPSC Cardiomyocyte 3D Spheroids. SLAS Discov. *26*, 352–363.
53. Bargehr, J., Ong, L.P., Colzani, M., Davaapil, H., Hofsteen, P., Bhandari, S., Gambardella, L., Le Novère, N., Iyer, D., Sampaziotis, F., et al. (2019). Epicardial cells derived from human embryonic stem cells augment cardiomyocyte-driven heart regeneration. Nat. Biotechnol. *37*, 895–906.
54. Cho, G.S., Lee, D.I., Tampakakis, E., Murphy, S., Andersen, P., Uosaki, H., Chelko, S., Chakir, K., Hong, I., Seo, K., et al. (2017). Neonatal Transplantation Confers Maturation of PSC-Derived Cardiomyocytes Conducive to Modeling Cardiomyopathy. Cell Rep. *18*, 571–582.
55. Baehr, A., Umansky, K.B., Bassat, E., Jurisch, V., Klett, K., Bozoglu, T., Hornaschewitz, N., Solyanik, O., Kain, D., Ferraro, B., et al. (2020). Agrin Promotes Coordinated Therapeutic Processes Leading to Improved Cardiac Repair in Pigs. Circulation *142*, 868–881.
56. Yokoyama, J., Miyagawa, S., Akagi, T., Akashi, M., and Sawa, Y. (2021). Human induced pluripotent stem cell-derived three-dimensional cardiomyocyte tissues ameliorate the rat ischemic myocardium by remodeling the extracellular matrix and cardiac protein phenotype. PLoS One *16*, e0245571.
57. Wang, Y., Yao, F., Wang, L., Li, Z., Ren, Z., Li, D., Zhang, M., Han, L., Wang, S.Q., Zhou, B., and Wang, L. (2020). Single-cell analysis of murine fibroblasts identifies neonatal to adult switching that regulates cardiomyocyte maturation. Nat. Commun. *11*, 2585.
58. Block, T., Creech, J., da Rocha, A.M., Marinkovic, M., Ponce-Balbuena, D., Jiménez-Vázquez, E.N., Griffey, S., and Herron, T.J. (2020). Human perinatal stem cell derived extracellular matrix enables rapid maturation of hiPSC-CM structural and functional phenotypes. Sci. Rep. *10*, 19071.
59. Robert, A.W., Pereira, I.T., Dallagiovanna, B., and Stimamiglio, M.A. (2020). Secretome Analysis Performed During in vitro Cardiac Differentiation: Discovering the Cardiac Microenvironment. Front. Cell Dev. Biol. *8*, 49.
60. Kobayashi, T., Nguyen-Tien, D., Sorimachi, Y., Sugiura, Y., Suzuki, T., Karyu, H., Shimabukuro-Demoto, S., Uemura, T., Okamura, T., Taguchi, T., et al. (2021). SLC15A4 mediates M1-prone metabolic shifts in macrophages and guards immune cells from metabolic stress. Proc. Natl. Acad. Sci. USA *118*. e2100295118.
61. Kim, D.I., Lim, S.K., Park, M.J., Han, H.J., Kim, G.Y., and Park, S.H. (2007). The involvement of phosphatidylinositol 3-kinase/Akt signaling in high glucose-induced downregulation of GLUT-1 expression in ARPE cells. Life Sci. *80*, 626–632.
62. Gao, Y.Y., Chen, L., Wang, T., Nie, Z.W., Zhang, X., and Miao, Y.L. (2016). Oocyte aging-induced Neuronatin (NNAT) hypermethylation affects oocyte quality by impairing glucose transport in porcine. Sci. Rep. *6*, 36008.
63. Morita, Y., and Tohyama, S. (2020). Metabolic Regulation of Cardiac Differentiation and Maturation in Pluripotent Stem Cells: A Lesson from Heart Development. JMA J *3*, 193–200.
64. Jayadev, R., Morais, M.R.P.T., Ellingford, J.M., Srinivasan, S., Naylor, R.W., Lawless, C., Li, A.S., Ingham, J.F., Hastie, E., Chi, Q., et al. (2022). A basement membrane discovery pipeline uncovers network complexity, regulators, and human disease associations. Sci. Adv. *8*, eabn2265.
65. Ocken, A.R., Ku, M.M., Kinzer-Ursem, T.L., and Calve, S. (2020). Perlecan Knockdown Significantly Alters Extracellular Matrix Composition and Organization During Cartilage Development. Mol. Cell. Proteomics *19*, 1220–1235.
66. Nonaka, R., Iesaki, T., Kerever, A., and Arikawa-Hirasawa, E. (2021). Increased Risk of Aortic Dissection with Perlecan Deficiency. Int. J. Mol. Sci. *23*, 315.
67. Zhao, Y., Rafatian, N., Wang, E.Y., Feric, N.T., Lai, B.F.L., Knee-Walden, E.J., Backx, P.H., and Radisic, M. (2020). Engineering microenvironment for human cardiac tissue assembly in heart-on-a-chip platform. Matrix Biol. *85–86*, 189–204.
68. Tzahor, E., and Dimmeler, S. (2022). A coalition to heal-the impact of the cardiac microenvironment. Science *377*, eabm4443.
69. Yahalom-Ronen, Y., Rajchman, D., Sarig, R., Geiger, B., and Tzahor, E. (2015). Reduced matrix rigidity promotes neonatal cardiomyocyte dedifferentiation, proliferation and clonal expansion. Elife *4*, e07455.
70. Pei, S., Parthasarathy, S., Parajuli, A., Martinez, J., Lv, M., Jiang, S., Wu, D., Wei, S., Lu, X.L., Farach-Carson, M.C., et al. (2020). Perlecan/Hspg2 deficiency impairs bone’s calcium signaling and associated transcriptome in response to mechanical loading. Bone *131*, 115078.
71. Sharma, J., Mukherjee, D., Rao, S.N.R., Iyengar, S., Shankar, S.K., Satishchandra, P., and Jana, N.R. (2013). Neuronatin-mediated aberrant calcium signaling and endoplasmic reticulum stress underlie neuropathology in Lafora disease. J. Biol. Chem. *288*, 9482–9490.
72. Joseph, R., Dou, D., and Tsang, W. (1994). Molecular cloning of a novel mRNA (neuronatin) that is highly expressed in neonatal mammalian brain. Biochem. Biophys. Res. Commun. *201*, 1227–1234.
73. Joseph, R., Dou, D., and Tsang, W. (1995). Neuronatin mRNA: alternatively spliced forms of a novel brain-specific mammalian developmental gene. Brain Res. *690*, 92–98.
74. Zebrowski, D.C., and Engel, F.B. (2013). The cardiomyocyte cell cycle in hypertrophy, tissue homeostasis, and regeneration. Rev. Physiol. Biochem. Pharmacol. *165*, 67–96.
75. Yuan, X., and Braun, T. (2017). Multimodal Regulation of Cardiac Myocyte Proliferation. Circ. Res. *121*, 293–309.
76. Vliegen, H.W., Eulderink, F., Bruschke, A.V., van der Laarse, A., and Cornelisse, C.J. (1995). Polyploidy of myocyte nuclei in pressure overloaded human hearts: a flow cytometric study in left and right ventricular myocardium. Am. J. Cardiovasc. Pathol. *5*, 27–31.
77. Brodsky, V., Sarkisov, D.S., Arefyeva, A.M., Panova, N.W., and Gvasava, I.G. (1994). Polyploidy in cardiac myocytes of normal and hypertrophic human hearts; range of values. Virchows Arch. *424*, 429–435.
78. Schneider, R., and Pfitzer, P. (1972). [Number of nuclei in isolated human myocardial cells]. Virchows Arch. B Cell Pathol. *12*, 238–258.
79. Yamamoto, K., Ohki, R., Lee, R.T., Ikeda, U., and Shimada, K. (2001). Peroxisome proliferator-activated receptor gamma activators inhibit cardiac hypertrophy in cardiac myocytes. Circulation *104*, 1670–1675.

80. Johansson, M., Ulfenborg, B., Andersson, C.X., Heydarkhan-Hagvall, S., Jeppsson, A., Sartipy, P., and Synnergren, J. (2022). Multi-Omics Characterization of a Human Stem Cell-Based Model of Cardiac Hypertrophy. Life *12*, 293.

81. Xu, Z., Ichikawa, N., Kosaki, K., Yamada, Y., Sasaki, T., Sakai, L.Y., Kurosawa, H., Hattori, N., and Arikawa-Hirasawa, E. (2010). Perlecan deficiency causes muscle hypertrophy, a decrease in myostatin expression, and changes in muscle fiber composition. Matrix Biol. *29*, 461–470.

82. Boland, E., Quondamatteo, F., and Van Agtmael, T. (2021). The role of basement membranes in cardiac biology and disease. Biosci. Rep. *41*.

83. Farach-Carson, M.C., and Carson, D.D. (2007). Perlecan–a multifunctional extracellular proteoglycan scaffold. Glycobiology *17*, 897–905.

84. Ritchie, S., Pereira, B.A., Vennin, C., and Timpson, P. (2020). Targeting genetically-tuned CAFs in pancreatic cancer via perlecan manipulation. Expert Opin. Ther. Targets *24*, 171–174.

85. Vallier, L., Alexander, M., and Pedersen, R.A. (2005). Activin/Nodal and FGF pathways cooperate to maintain pluripotency of human embryonic stem cells. J. Cell Sci. *118*, 4495–4509.

86. Xu, C., Rosler, E., Jiang, J., Lebkowski, J.S., Gold, J.D., O'Sullivan, C., Delavan-Boorsma, K., Mok, M., Bronstein, A., and Carpenter, M.K. (2005). Basic fibroblast growth factor supports undifferentiated human embryonic stem cell growth without conditioned medium. Stem Cell. *23*, 315–323.

87. Chen, G., Gulbranson, D.R., Hou, Z., Bolin, J.M., Ruotti, V., Probasco, M.D., Smuga-Otto, K., Howden, S.E., Diol, N.R., Propson, N.E., et al. (2011). Chemically defined conditions for human iPSC derivation and culture. Nat. Methods *8*, 424–429.

88. Aviezer, D., Hecht, D., Safran, M., Eisinger, M., David, G., and Yayon, A. (1994). Perlecan, basal lamina proteoglycan, promotes basic fibroblast growth factor-receptor binding, mitogenesis, and angiogenesis. Cell *79*, 1005–1013.

89. Chang, Y.T., Tseng, C.N., Tannenberg, P., Eriksson, L., Yuan, K., de Jesus Perez, V.A., Lundberg, J., Lengquist, M., Botusan, I.R., Catrina, S.B., et al. (2015). Perlecan heparan sulfate deficiency impairs pulmonary vascular development and attenuates hypoxic pulmonary hypertension. Cardiovasc. Res. *107*, 20–31.

90. Vincent, T.L., McLean, C.J., Full, L.E., Peston, D., and Saklatvala, J. (2007). FGF-2 is bound to perlecan in the pericellular matrix of articular cartilage, where it acts as a chondrocyte mechanotransducer. Osteoarthritis Cartilage *15*, 752–763.

91. Kerever, A., Mercier, F., Nonaka, R., de Vega, S., Oda, Y., Zalc, B., Okada, Y., Hattori, N., Yamada, Y., and Arikawa-Hirasawa, E. (2014). Perlecan is required for FGF-2 signaling in the neural stem cell niche. Stem Cell Res. *12*, 492–505.

92. Ronaldson-Bouchard, K., Ma, S.P., Yeager, K., Chen, T., Song, L., Sirabella, D., Morikawa, K., Teles, D., Yazawa, M., and Vunjak-Novakovic, G. (2018). Advanced maturation of human cardiac tissue grown from pluripotent stem cells. Nature *556*, 239–243.

93. Whitelock, J.M., Graham, L.D., Melrose, J., Murdoch, A.D., Iozzo, R.V., and Underwood, P.A. (1999). Human perlecan immunopurified from different endothelial cell sources has different adhesive properties for vascular cells. Matrix Biol. *18*, 163–178.

94. Kondrashov, A., Duc Hoang, M., Smith, J.G.W., Bhagwan, J.R., Duncan, G., Mosqueira, D., Munoz, M.B., Vo, N.T.N., and Denning, C. (2018). Simplified Footprint-Free Cas9/CRISPR Editing of Cardiac-Associated Genes in Human Pluripotent Stem Cells. Stem Cells Dev. *27*, 391–404.

95. Sala, L., van Meer, B.J., Tertoolen, L.G.J., Bakkers, J., Bellin, M., Davis, R.P., Denning, C., Dieben, M.A.E., Eschenhagen, T., Giacomelli, E., et al. (2018). MUSCLEMOTION: A Versatile Open Software Tool to Quantify Cardiomyocyte and Cardiac Muscle Contraction In Vitro and In Vivo. Circ. Res. *122*, e5–e16.

96. Burridge, P.W., Matsa, E., Shukla, P., Lin, Z.C., Churko, J.M., Ebert, A.D., Lan, F., Diecke, S., Huber, B., Mordwinkin, N.M., et al. (2014). Chemically defined generation of human cardiomyocytes. Nat. Methods *11*, 855–860.

97. Smith, J.G.W., Owen, T., Bhagwan, J.R., Mosqueira, D., Scott, E., Mannhardt, I., Patel, A., Barriales-Villa, R., Monserrat, L., Hansen, A., et al. (2018). Isogenic Pairs of hiPSC-CMs with Hypertrophic Cardiomyopathy/LVNC-Associated ACTC1 E99K Mutation Unveil Differential Functional Deficits. Stem Cell Rep. *11*, 1226–1243.

98. Li, B., and Dewey, C.N. (2011). RSEM: accurate transcript quantification from RNA-Seq data with or without a reference genome. BMC Bioinf. *12*, 323.

99. Soneson, C., Love, M.I., and Robinson, M.D. (2015). Differential analyses for RNA-seq: transcript-level estimates improve gene-level inferences. F1000Res. *4*, 1521.

100. Love, M.I., Huber, W., and Anders, S. (2014). Moderated estimation of fold change and dispersion for RNA-seq data with DESeq2. Genome Biol. *15*, 550.

101. Stephens, M. (2017). False discovery rates: a new deal. Biostatistics *18*, 275–294.

102. Benjamini, Y., and Cohen, R. (2017). Weighted false discovery rate controlling procedures for clinical trials. Biostatistics *18*, 91–104.

103. Gu, Z., Eils, R., and Schlesner, M. (2016). Complex heatmaps reveal patterns and correlations in multidimensional genomic data. Bioinformatics *32*, 2847–2849.

104. Wu, T., Hu, E., Xu, S., Chen, M., Guo, P., Dai, Z., Feng, T., Zhou, L., Tang, W., Zhan, L., et al. (2021). clusterProfiler 4.0: A universal enrichment tool for interpreting omics data. Innovation *2*, 100141.

105. Ashburner, M., Ball, C.A., Blake, J.A., Botstein, D., Butler, H., Cherry, J.M., Davis, A.P., Dolinski, K., Dwight, S.S., Eppig, J.T., et al. (2000). Gene ontology: tool for the unification of biology. The Gene Ontology Consortium. Nat. Genet. *25*, 25–29.

106. Subramanian, A., Tamayo, P., Mootha, V.K., Mukherjee, S., Ebert, B.L., Gillette, M.A., Paulovich, A., Pomeroy, S.L., Golub, T.R., Lander, E.S., and Mesirov, J.P. (2005). Gene set enrichment analysis: a knowledge-based approach for interpreting genome-wide expression profiles. Proc. Natl. Acad. Sci. USA *102*, 15545–15550.

107. Mootha, V.K., Lindgren, C.M., Eriksson, K.F., Subramanian, A., Sihag, S., Lehar, J., Puigserver, P., Carlsson, E., Ridderstråle, M., Laurila, E., et al. (2003). PGC-1alpha-responsive genes involved in oxidative phosphorylation are coordinately downregulated in human diabetes. Nat. Genet. *34*, 267–273.

108. Kuppusamy, K.T., Jones, D.C., Sperber, H., Madan, A., Fischer, K.A., Rodriguez, M.L., Pabon, L., Zhu, W.Z., Tulloch, N.L., Yang, X., et al. (2015). Let-7 family of microRNA is required for maturation and adult-like metabolism in stem cell-derived cardiomyocytes. Proc. Natl. Acad. Sci. USA *112*, E2785–E2794.

109. Dobin, A., Davis, C.A., Schlesinger, F., Drenkow, J., Zaleski, C., Jha, S., Batut, P., Chaisson, M., and Gingeras, T.R. (2013). STAR: ultrafast universal RNA-seq aligner. Bioinformatics *29*, 15–21.

110. Marchi, S., Bonora, M., Patergnani, S., Giorgi, C., and Pinton, P. (2017). Methods to Assess Mitochondrial Morphology in Mammalian Cells Mounting Autophagic or Mitophagic Responses. Methods Enzymol. *588*, 171–186.

111. Ripmeester, E.G.J., Caron, M.M.J., van den Akker, G.G.H., Surtel, D.A.M., Cremers, A., Balaskas, P., Dyer, P., Housmans, B.A.C., Chabronova, A., Smagul, A., et al. (2020). Impaired chondrocyte U3 snoRNA expression in osteoarthritis impacts the chondrocyte protein translation apparatus. Sci. Rep. *10*, 13426.

112. Peffers, M.J., Thorpe, C.T., Collins, J.A., Eong, R., Wei, T.K.J., Screen, H.R.C., and Clegg, P.D. (2014). Proteomic analysis reveals age-related changes in tendon matrix composition, with age- and injury-specific matrix fragmentation. J. Biol. Chem. *289*, 25867–25878.

## STAR★METHODS

### KEY RESOURCES TABLE

| REAGENT or RESOURCE | SOURCE | IDENTIFIER |
|---|---|---|
| Antibodies | | |
| Anti-Heparan Sulfate Proteoglycan 2/Perlecan antibody [A74] (1:200) | Abcam | CAT# AB23418: RRID:AB_2119099 |
| Anti-Heparan Sulfate Proteoglycan 2/Perlecan antibody [A76] (1:1000) | Abcam | CAT# AB26265: RRID:AB_470833 |
| Anti-Heparan Sulfate Proteoglycan 2/Perlecan antibody [CCN1] (1:2000) | Provided by John Whitelock, (Whitelock et al.)[93] | N/A |
| Anti-Agrin Primary Antibody (1:200) | Thermo Fisher Scientific | CAT# 103585: RRID:AB_2852921 |
| Goat Anti-Rabbit IgG H&L (Alexa Fluor® 568) (1:500) | Abcam | CAT# AB175471: RRID:AB_2576207 |
| Goat Anti-Mouse IgG H&L (Alexa Fluor® 568) (1:500) | Abcam | CAT# AB175473: RRID:AB_2895153 |
| Goat Anti-Mouse IgG H&L HRP | Abcam | CAT# AB6728: RRID:AB_955440 |
| Goat Anti-Rabbit IgG H&L HRP | Abcam | CAT# AB6721: RRID:AB_955447 |
| Bacterial and virus strains | | |
| Top10 Chemically Competent *E.coli* | Thermo Fisher Scientific | C404010 |
| Chemicals, peptides, and recombinant proteins | | |
| Essential 8 Medium | Gibco Life Technologies | A1516901 |
| Essential 8 Supplement (50X) | Gibco Life Technologies | A1517101 |
| Matrigel hESC-Qualified Matrix | Corning | 354277 |
| Vitronectin, truncated recombinant human (VTN-N) | Thermo Fisher Scientific | A14700 |
| TrypLE Select | Gibco | 12604021 |
| CHIR 99021 | Selleck Chemicals | S2924 |
| IWR-1 | Sigma-Aldrich | I0161-25MG |
| AGN 193109 SODIUM SALT | Santa Cruz Biotechnology | sc-210768 |
| Recombinant Human BMP4 | R&D Systems | 314-BP-010 |
| Recombinant Human FGF-2 | R&D Systems | 233-FB-025 |
| Human Activin A | R&D Systems | 338-AC-010 |
| RPMI 1640 | Gibco Life Technologies | 11875 |
| RPMI 1640 Medium, No Glucose | Gibco Life Technologies | 11879020 |
| B27 Supplement 50X | Gibco Life Technologies | 17504044 |
| B27 -insulin Supplement 50X | Gibco Life Technologies | A1895601 |
| B27 -VitaminA Supplement 50X | Gibco Life Technologies | 12587010 |
| Fetal Bovine Serum (FBS), Qualified, Heat Inactivated | Gibco | 16140071 |
| Horse Serum | Gibco | 26050 |
| Agarose | Invitrogen | BP1356-100 |
| Goat Serum | Sigma-Aldrich | G9023 |
| DAPI | Thermo Fisher Scientific | 62248 |
| Fibrinogen | Sigma-Aldrich | F4753 |
| Thrombin | Sigma-Aldrich | 1123740001 |
| Formaldehyde Solution 4%, Buffered, Ph 6.9 | Sigma-Aldrich | P6148 |

(*Continued on next page*)

***Continued***

| REAGENT or RESOURCE | SOURCE | IDENTIFIER |
|---|---|---|
| BioLog MAS | BioLog | 72303 |
| BioLog MitoPlate S-1 | BioLog | 14105 |
| BioLog Redox Dye Mix MC | BioLog | 74353 |
| Saponin | Sigma-Aldrich | 47036-50G-F |
| ECL Extra | Expedeon | ECLA0250 |
| ECL Extreme | Expedeon | ECLM0100 |
| Milk Powder | Thermo Fisher Scientific | 16694685 |
| Precision Plus Protein Standards Dual Color Prestained Ladder | Bio-Rad | 161–0374 |
| SDS Solution, 10% Sodium Dodecyl Sulfate Solution | Thermo Fisher Scientific | 151-21-3 |
| Tris-Base | Sigma-Aldrich | 77-86-1 |
| Transblot Turbo Mini-Size Nitrocellulose | BioRad | 1704156 |
| Transblot Turbo Mini-Size Transfer Stacks | BioRad | 1704158 |
| Triton X-100 Solution | Sigma-Aldrich | 93443-100ML |
| TWEEN 20 | Sigma-Aldrich | P1379-100ML |
| Revert 700 Total Protein Stain | LI-COR Biosciences | 926–11011 |
| Proteinase K | Thermo Fisher Scientific | EO0491 |
| Gel Loading Dye Purple (6X) | New England BioLabs | B7024S |
| Generuler 1kb DNA Ladder | Thermo Fisher Scientific | SM0311 |
| Blasticidin | Tocris | 5502 |
| Y-27632 (ROCK Inhibitor) | MedChemExpress | HY-10583 |
| Penicillin-Streptomycin | Gibco | 15140122 |
| Phosphate Buffered Saline (Pbs) Tablets | Gibco | 18912014 |
| Phusion High-Fidelity DNA Polymerase | New England BioLabs | M0530L |
| SYBR Safe DNA Gel Stain | Invitrogen | S33102 |
| Collagenase Type 2 | Worthington Biochem | LS004174 |
| Critical commercial assays | | |
| P3 Primary Cell 4D-Nucleofector® X Kit | Lonza | V4XP-3024 |
| Seahorse XFP Cell Mito Stress Test Kit | Agilent | 103010–100 |
| qPCRBio cDNA Synthesis Kit | PCR Biosystems | PB30.11–10 |
| qPCRBio SyGreen Mix Lo-Rox | PCR Biosystems | PB20.11–05 |
| RNeasy Micro Kit | Qiagen | 74104 |
| denovoMATRIX Synthetic Perlecan Peptide Plates | denovoMATRIX | N/A |
| Deposited data | | |
| Gene expression HSPG2 cell line (bulk RNA-seq) | This paper | GEO: GSE229975 |
| Gene expression ACTN2-GFP-hPSC cell line (bulk RNA-seq) | (Dark et al.)[27] | GEO: GSE203375 |
| Experimental models: Cell lines | | |
| ACTN2-GFP-hPSC line | Allen Institute | AICS-0075-085 |
| ACTN2-HSPG2+/− hPSC line | This Study | HSPG2$^{+/-}$ |
| Oligonucleotides | | |
| *See* Table S1 *for list of oligonucleotides* | Sigma Aldrich | N/A |
| Recombinant DNA | | |
| HSPG2 Guide RNA | (Kondrashov et al.)[94] | N/A |
| CRISPR/Cas9 | (Kondrashov et al.)[94] | N/A |
| Software and algorithms | | |
| GraphPad Prism 5.0 | GraphPad Prism | N/A |
| Fiji-ImageJ | Fiji | https://ImageJ.net/Fiji/Downloads |

(*Continued on next page*)

***Continued***

| REAGENT or RESOURCE | SOURCE | IDENTIFIER |
|---|---|---|
| MUSCLEMOTION | (Sala et al.)[95] | |
| RStudio | RStudio | https://rstudio.com/products/rstudio |
| Snapgene Viewer | Snapgene | N/A |
| Data Analysis 1.7 | BioLog Data Analysis 1.7 | N/A |
| Harmony | PerkinElmer | N/A |
| Adobe Illustrator | Adobe Illustrator | N/A |

## RESOURCE AVAILABILITY

### Lead contact

Further information and requests for resources and reagents should be directed to and will be fulfilled by the Lead Contact, Dr. James G.W. Smith (J.G.Smith@uea.ac.uk).

### Materials availability

Perlecan mutant hiPSC lines are available upon request and under an MTA. Plasmids used to generate these lines are also available upon request and under an MTA and will be deposited to addgene to be made publicly available as of the date of publication.

### Data and code availability

(1) RNA-seq data have been deposited at GEO and are publicly available as of the date of publication. The accession numbers for the bulk RNA sequencing datasets reported in this paper are GEO: GSE203375 and GSE229975. Proteomic data are available via ProteomeXchange with the identifier Project www.doi.org/10.6019/PXD046359. Microscopy data reported in this paper will be shared by the lead contact upon request.

(2) All original code has been deposited at GitHub and is publicly available as of the date of publication. RNA sequencing alignment https://github.com/nf-core/rnaseq.

(3) Any additional information required to reanalyze the data reported in this paper is available from the lead contact upon request.

## EXPERIMENTAL MODEL AND STUDY PARTICIPANT DETAILS

### Ethics statement

Protocols for research involving human stem cell research were approved by the medical ethical committee at the University of East Anglia, UK, the bio-safety committee at Imperial College London, UK, and the UK Stem Cell Bank steering committee.

All mouse studies were performed under a UK Home Office project license and complied fully with the UK Animals (Scientific Procedures) Act 1986, amended 2012 (ASPA), as implemented by the Francis Crick Institute.

### hPSC lines origin, characterization and maintenance

ACTN2-GFP-hPSC line was purchased from the Allen Institute (AICS-0075-085, sex: male, karyotype and certificate of analysis available). The HSPG2$^{+/-}$ hPSC line was generated from the ACTN2-GFP-hPSC through nucleofector electroporation (Lonza 4D, program CA-137) of (1 μg total DNA) and homologous recombination followed by antibiotic selection. The ACTN2-GFP-hPSC line was further validated through PCR, real-time PCR and western blotting (Figure S1). All hPSC lines were seeded on vitronectin recombinant human protein and cultured in E8 medium in a humidified atmosphere (5% CO2) at 37°C. Cells were passaged twice a week using TrylpLE Select (1X) and E8 supplemented with 10 μM Y-27632 Rho kinase inhibitor (MedChemExpress). Human stem cells were subject to routine pluripotency testing using BD Stemflow Human and Mouse Pluripotent Stem Cell Analysis Kit (BD Biosciences) as recommended by the manufacturers, or by immunostaining against OCT3/4, SOX2 and NANOG using the standard immunostaining protocol as detailed below. In house routine low-pass sequencing was also performed to confirm karyotype stability.

### Mouse embryo collections

CD1 mice were time mated for embryo collections at P0, P2, P7 and P10 (entire litter comprising both male and female mice). Animals were culled by cervical dislocation and hearts were microdissected in flushing and handling media (FHM: DMEM-pyruvate free with HEPES), quickly washed in PBS, and either snap frozen on dry ice for Western blot analysis or frozen in OCT, also on dry ice, for cryosection. Samples were stored at −80°C until ready for follow up processing/analysis.

### Human tissues

No human tissues were collected purposedly for this work. All human tissue RNA-sequencing was reanalysed from previously published sources (See resource table).

## METHOD DETAILS

### Cardiomyocyte differentiation from hPSCs and generation of 3D engineered heart tissue (EHT)

The cardiomyocyte differentiation protocol was adapted from Burridge et al. 2014[96] to promote left ventricle cardiomyocyte differentiation.[27] A patent has been granted for this method: WO2020245612. Briefly, this method uses RPMI supplemented with B27 - insulin, AGN Sodium Salt (Santa Cruz Biotechnology), CHIR99021 (3 μM, Selleck Chemicals), BMP4 (3 ng/mL, R&D Systems), Activin A (5 ng/mL, R&D Systems) and FGF2 (5 ng/mL, R&D Systems) for 24 h, followed by 48 h with RPMI/B27- insulin supplemented with IWR-1 (1 μM, Tocris). This produced spontaneous contracting early cardiomyocytes by day (D) 6. These are directed to ventricular specification (D6-10) using RMPI/B27 – Vitamin A (Life Technologies), followed by metabolic selection (D10-14) using RPMI – glucose/B27 – Vitamin A, supplemented with L-Lactic acid (4 mM, Sigma). Finally, a period of *in-vitro* maturation (D14-30) in RMPI/B27, on a vitronectin peptide coated surfaces (VTN). To investigate perlecan signaling during maturation, hPSC-CMs were re-plated on a perlecan peptide coated substrate (denovoMATRIX) for the final 10 days of maturation and compared to hPSC-CMs re-plated on vitronectin peptide controls.

EHTs were fabricated as previously described.[95,97] In brief, Teflon spacers (EHT Technologies) were inserted in 2% ultra-pure agarose (Invitrogen) solution in 24-well plates (Nunc) to form apertures. Silicone racks (EHT Technologies) were placed in the aperture and $1x10^6$ freshly dissociated hPSC-CMs were resuspended in media containing 5 mg/mL fibrinogen (Sigma) followed by the addition of 3 U of thrombin (Sigma). Forming EHTs were then incubated for 2 h at 37°C and subsequently moved to new 24-well plates filled with DMEM supplemented with 10% horse serum (Gibco), 10 mg/mL insulin (Sigma), 33 mg/mL aprotinin (Sigma), and 1% (v/v) PEST, termed EHT media. EHTs were fed every other day for 14 days before contraction analysis using MUSCLEMOTION software.[95]

### Cardiomyocyte dissociation and replating

Cardiomyocytes were re-plated usually between days 14–16 using the cardiomyocyte dissociation medium from STEMCELL Technologies and following manufacturer's guidelines (STEMCELL Technologies). Cells were plated onto new dishes in cardiomyocyte support medium (STEMCELL Technologies) supplemented with 10 μM Y-27632 (Tocris). 24 h post re-plating, media was changed to the cardiomyocyte maintenance media. For some experiments, e.g., EHT generation, cardiomyocyte dissociation was performed alternatively in collagenase as previously described.[95,97]

### Gene expression (real-time PCR)

RNA was extracted from cells using Qiazol (Qiagen) following the manufacturer's instructions. Quantitative real-time PCR analysis was performed using a Roche LightCycler 480 II. Reverse transcription was performed of RNA using the Ultrascript 2.0 cDNA Synthesis Kit (PCR Biosystems). Reactions contained 1 μL cDNA, 2.5 μL SYBR Green PCR Master Mix (PCR Biosystems), 0.5 μL primer master mix and 1 μL H2O. All real-time PCR reactions were performed in triplicate, normalised to housekeeper gene GAPDH and assessed using a comparative Ct method. Primer sequences are shown in Table 1.

### Gene expression (bulk RNA-sequencing)

Whole-genome transcriptome data were generated at The Francis Crick Institute (London, United Kingdom) using the Illumina Hiseq4000 (100bp reads). Samples were run through the nf-core RNAseq pipeline (https://github.com/nf-core/rnaseq, version 3.8.1) using the STAR aligner to align to human genome build GRCh38 (release-95), with RSEM quantification.[98] Results were processed in R (version 4.2.0). Genes with an effective length of zero for all samples were amended to a length of one to avoid errors in downstream analysis. All non-integer counts were rounded down.Gene-level estimated counts and average transcript lengths were imported into R using the tximport package[99] and analyzed for differential gene expression using the the default methods of DESeq2.[100] Variance stabilising transformation (VST-normalisation) was applied for all visualisations, and log2 fold change (LFC) shrinkage using the ashr method[101] was applied prior to gene ranking. VST-normalized data was subjected to principal component analysis (via DESeq2, https://github.com/mikelove/DESeq2), correlation analysis, and assessment of genes with highest variance (via R base stats package), to discover any unaccounted for structure in the data. Following this assessment, an analysis design was settled on that accounted for time, genotype and replicate (formula used: ~ genotype + timepoint + genotype:replicate + genotype:timepoint).

### Differential expression and further data exploration

Differential gene expression analysis was assessed using DESeq2's Wald test between the Heterozygous KO and WT genotypes at each timepoint, and between all pairs of consecutive time-points for each genotype. Genes that did not converge in beta were removed. Benjamini-Hochberg correction[102] was used to control for the false-discovery rate. Genes were called as significant if they passed a combined filter of i) FDR<0.01, ii) absolute fold change >2 and iii) base-mean >30. Significant genes from each comparison were combined for visualisation as a heatmap[103] and against a background of other genes in MA plots (ggplot2 3.3.6, H. Wickham. ggplot2: Elegant Graphics for Data Analysis. Springer-Verlag New York, 2016.). Genes differentially expressed across time-points were identified using Likelihood Ratio Test (LRT, via DESeq2), removing the interaction of genotype and time to create the reduced design formula (full: as above, reduced: ~ genotype + timepoint + genotype:replicate). Volcano plots were generated using Enhanced Volcano (https://github.com/kevinblighe/EnhancedVolcano) library package from Bioconductor with pCutoff set to 0.05.

## Gene set enrichment analysis

Over-representation analyses (ORA) were performed using clusterProfiler (version 4.4.4),[104] against terms in the Biological Processes (BP), Molecular Functions (MF), Cellular Components (CC), KEGG and Reactome (REAC) domain of The GO Consortium.[105] Genes with a significant fold change (adjusted p value <0.05) and a non-zero baseMean were ordered by decreasing ashr-shrunken LFC and assessed using the enrichGO function (clusterProfiler) against a universe of all genes detected in that sample. Gene Set Enrichment Analyses (GSEA)[106,107] were performed using the gseGO function (clusterProfiler) on gene lists per DESeq2 contrast, ordered by decreasing ashr-shrunk LFC, against BP, MF, CC, KEGG and REAC terms. For both ORA and GSEA, a p.value and q.value cutoff of 0.05 was used, and p.values were adjusted according to Benjamini-Hochberg methods.

## Gene expression heatmaps

Heatmaps were generated (ComplexHeatmap, https://github.com/jokergoo/ComplexHeatmap) to show the expression of a set of maturity genes.[108] Expression was scaled by subtracting the median expression per gene from each samples' expression for that gene. Heatmap rows were ordered according to the Ward.D2 (base R stats package, 4.2.0) method of general agglomerative hierarchical clustering.

## Differential transcript analysis

Differential transcript usage was calculated by performing DESeq2 analysis on isoform data output from the nf-core pipeline, using the same parameters as described above, and a nonlinear form of the model that allowed 'timepoint' three knots in all instances in the design. Results were VST-normalised and LFCs were shrunken as above. Contrasts were made between genotypes and timepoints, and the full model was compared to a reduced model excluding 'genotype:timepoint'. Transcript IDs for *HSPG2* and *AGRN* were taken from the ensembl website (https://www.ensembl.org/Homo_sapiens/Info/Index).

## Comparison to existing hPSC-CM bulk RNA-sequencing data

Bulk samples were obtained from dataset GEO: GSE203375.[27] For comparisons across datasets, count files were joined into one unified dataset and analyzed using DESeq2 default methods and the following design formula: ~ genotype + timepoint + genotype:replicate + genotype: timepoint. Genes that did not converge in beta were removed, data was VST-normalised prior to visualisation via ggplot2.

## Comparison to existing human tissues bulk RNA-sequencing data

Gene count data from different sources were combined with our hPSC-CM data into one dataset for comparison: adult human left ventricle isolated cells (from GEO series GSE204885, published in 27); fetal human ventricular cells (GEO samples GSM1536186 and GSM1536187, published in 108); three WT samples from this paper, and three HSPG2$^{+/-}$ samples from this paper. All samples were aligned to GRCh38, which involved re-processing the fetal human ventricular data since this was originally aligned to hg19. The fetal data was aligned to GRCh38 via the nf-core RNAseq pipeline (https://github.com/nf-core/rnaseq, version 3.8.1) using STAR aligner to align to human genome build GRCh38 (release-95,[109]), with RSEM quantification.[98]

To combine these datasets, all gene counts were placed in one object and any non-integer counts were rounded down. A DESeq2 dataset was constructed using a design of ~1, and VST-normalisation was applied. This VST-normalised data was displayed as a PCA plot, following the calculation of principal components with plotPCA (https://github.com/kevinblighe/PCAtools). For axis labels, variance was multiplied by 100 to display as a percentage and rounded to the nearest integer.

The data was also displayed as a heatmap of the expression of 35 indicator genes representing eight ontologies from the GO and KEGG consortiums. VST-normalised data from the three sources was reduced to the 35 indicator genes, and gene expression across samples was scaled to the median for each gene. This data was plotted as a heatmap.

## Protein analysis

### *Immunocytochemistry*

For immunocytochemistry, hPSC-CMs were fixed for 15 min using 5% PFA (Sigma), permeabilised for 15 min in 0.1% Triton X-100 (Sigma), then blocked in 4% Goat Serum/PBS (Sigma) for 4 h. Primary antibodies were diluted in 4% Goat Serum/PBS and left overnight at 4°C. Primary antibodies used were c-terminus perlecan A74 (1:200 Abcam), n-terminus perlecan A76 (1:1000 Abcam), polyclonal perlecan CCN1 (1:2000 Whitelock et al.[93]), and agrin (1:200 Abcam). The following day, cells were washed with 0.1% Tween/PBS (PBST) (Sigma) followed by secondary antibody incubation using Alexa Fluor 568 (Abcam) diluted 1:500 in 4% Goat Serum/PBS (Sigma) for 1 h at room temperature. Cells were washed again with PBST followed by incubation with DAPI (Tocris) at 1:500 in PBS for 10 min.

### Immunostainng for high content imaging using Opera Phenix

Cells grown on black-rimed 96 well plates (Greiner Bio-One, 655090) were incubated with MitoTracker Deep Red (1:10,000) (Thermo Fisher Scientific, UK) in the dark for half an hour. Next, the mix was aspirated and cells were washed once with DPBS (-CaCl2, -MgCl2) (PBS) (Gibco, UK), followed by fixing cells with 4% paraformaldehyde Solution in PBS (4% PFA) (Boster, UK) for 15 min at room temperature. After washing cells with PBS twice, cells were kept in fresh PBS at 4°C in the dark until ready to be stained.

Immunocytochemistry started by removing the PBS and permeabilizing cells in PBS supplemented with 1 mL/L Triton X-100 (ABCAM, UK) (PBST solution) for 10 min at room temperature. After washing, cells were either stained with Cell Mask (Thermo Fisher Scientific, UK) in PBS solution (1:10,000) for 20 min at room temperature in the dark, or we proceeded straight to the blocking step. For blocking, cells were incubated with Blocking Buffer (5% Donkey Serum in PBS) for 1 h at room temperature. Next antibody master mixes were prepared with the primary antibodies (1:200 rabbit anti-Ki67, Abcam, Ab15580; and 1:500 rabbit anti-GFP, Abcam, Ab6556); these were made in 5% Donkey Serum in Gold Buffer (pH = 7.15, 10 mM Tris, 155 mM NaCl, 2 mM EGTA, 2mM MgCl2). Cells were incubated in antibody solutions overnight at 4°C. On the second day, antibody solutions were removed and cells were washed with PBS three times. Then, cells were incubated with Secondary Antibody Solution (5% Donkey Serum in Gold Buffer) (1:500 donkey Alexa-antibodies were used, Thermo Fisher Scientific) for 1 h at room temperature in the dark. After, cells were washed with PBS three times and next incubated with DAPI (1:10,000) (Thermo Fisher Scientific, UK) in PBS for 10 min in the dark. Lastly, cells were washed with PBS twice and ready to be analyzed in the Opera Phenix High Content Screening System (PerkinElmer). Imaging was done within 7 days of staining.

### OPERA phenix imaging and harmony analysis

The cells' phenotype was scanned using a ×40/NA 1.1 water lens. Z-stacks from $-1$ to 5 $\mu$m with a step size of 1 $\mu$m were acquired using excitation lasers at 405, 488, 568 and 640 nm and emission filters at 450, 540, 600 and 690 nm. The quantification and phenotype was analyzed using Harmony software 5.0 indicated in Table S4. First, segmentation of nuclei and cytoplasm was performed using DAPI and cell mask or mitochondrial channel after applying a smoothed filter. The peri-nucleus region was determined by a ring-region defined as 50% outer and 15% inner of the nucleus. Determination of actinin-positive cells was based on a cut-off baseline for actinin intensity per cell. Determination of Ki67-positive cells was conducted after Ki67 spot detection and final quantification as presented was based on the number of cells double-positive for both Ki67 and a-actinin. Determination of mitochondrial region was carried out through SER feature analysis. Form factor and aspect ratio formulation referred to the previous work of Marchi et al. 2017.[110]

### Western blotting

For western blotting, protein was extracted from cells using scraping and lysis with 100 $\mu$L of SDS-PAGE sample buffer supplemented with protease inhibitor cocktail (Sigma P8340, used at 1:100). Alternatively, snapped frozen cells were lysed in RIPA buffer. Snap frozen mouse hearts were also lysed in RIPA buffer using the Qiagen Tissue Lyser II, 2 min at 30 Hz, then placed on ice for 30 min and centrifuged for 10 min at 16 000 g. Cell lysates were quantified with BCA kit (Pierce) and 20 $\mu$g of protein were loaded onto a 4–15% or 4–20% gradient polyacrylamide gel (Bio-Rad or Genscript). hPSC derived samples were transferred to a nitrocellulose membrane (Bio-Rad) using the Trans-Blot Turbo transfer system (Bio-Rad) following the manufacturer's protocol. Mouse samples were wet transfered for 60 min at 100 V. Membranes were blocked in 5% milk in PBS (PBSM) or TBS (TBSM) for 1–4 h, then incubated with primary antibodies diluted in fresh PBSM or TBSM overnight at 4°C. Membranes were then washed with PBS or TBS +0.05% Tween (PBST, TBST), and incubated with secondary antibody (anti-mouse horseradish peroxidase, Invitrogen) at 1:2000-1:5000 in PBSM/TBSM for 1 h at room temperature. After washing with PBST/TBST, membranes were imaged using LumiBlue ECL Extreme substrate (Expedeon) on a CCD camera. Western blot for beta-catenin (CTNNB1, Sigma C2206-25UL) was used as a loading control.

### Label-Free liquid chromatography–tandem mass spectrometry (LC-MS/MS) analysis

Cell pellets were resuspended in a 25mM ammonium bicarbonate buffer (Sigma-Aldrich, 09830) supplemented with 7.5U of Benzonase nuclease (Merck Millipore, 70664-3) and protease inhibitor (Sigma-Aldrich, 11836170001). Samples were sonicated on ice and centrifuged. Supernatant was transferred to a new tube and protein concentration was determined by BCA assay (ThermoFisher, 23227).

In-solution tryptic digestion of the cell lysates was performed as previously described.[111] In short, 25 mM ammonium bicarbonate (Fluka Chemicals Ltd., Gillingham, UK) containing 0.05% (w/v) RapiGest (Waters, Elstree, UK) was added to 100 $\mu$g protein of each sample to produce a final volume of 160 $\mu$L and heated at 80°C for 10 min. DL dithiothreitol (Sigma-Aldrich) was added (3 mM final concentration) and incubated at 60°C for 10 min. Iodoacetamide (Sigma-Aldrich) was added (9 mM final concentration) and incubated at room temperature for 30 min in the dark. Tryptic digestion was undertaken using Lys-C endopeptidase (FUJIFILM Wako Pure Chemical, Osaka, Japan) at a ratio of 1:25 177 (enzyme:protein) and incubated at 37°C for 16 h, followed by a second trypsin supplementation for 2 h. Digestion was halted by the addition of trifluoroacetic acid (Sigma-Aldrich) to 0.5% (v/v final concentration) and rotation for 30 min at 37°C. Samples were centrifuged at 4 °C at 13,000 rpm for 10 min and the supernatant was removed. 1200 ng of each tryptic digest was analyzed using LC-MS/MS, on a 2 h gradient for the cellular proteome and a 30 min gradient for the ribosomal proteome. Data analyses were performed as previously described.[111]

## LC-MS/MS spectral acquisition

Samples were loaded onto the trapping column (Thermo Scientific, PepMap100, C18, 300 μm × 5 mm), using partial loop injection, for 7 min at a flow rate of 12 μL/min with 0.1% (v/v) FA. The sample was resolved on the analytical column (Easy-Spray C18 75 μm × 500 mm 2 μm column) using a gradient of 96.2% A (0.1% formic acid) 3.8% B (79.95% acetonitrile, 19.95% water, 0.1% formic acid) to 50% A 50% B over 90 min at a flow rate of 0.3 nL/min (2-h gradient), interspersed with 30min blanks between the samples. The data-dependent program used for data acquisition consisted of a 60,000-resolution full-scan MS scan in the orbitrap (AGC set to 3e6 ions with a maximum fill time of 100ms). The 16 most abundant peaks per full scan were selected for HCD MS/MS (30,000 resolution, AGC set to 1e5 ions with a maximum fill time of 45 ms) with an ion selection window of 2 m/z and normalised collision energy of 30%. Ion selection excluded singularly charged ions and ions with equal to or a greater than +6 charge state. To avoid repeated selection of peptides for fragmentation the program used a 60-s dynamic exclusion window. All samples were analyzed in random order.

## Peptide identification and quantification

For peptide/protein database searches we used an in-house Mascot server. Unihuman reviewed database was used with search parameters including the following: peptide mass tolerance, 10.0 ppm; fragment mass tolerance, 0.01 Da; enzyme, trypsin; missed cleavages allowed, one; fixed modifications, carbamidomethylation (cysteine) and variable modifications; oxidation(methionine).

## Label-free quantification

The Progenesis QI software (V4, Waters) was used for protein quantification (only unique peptides were considered).[112] Data are available via ProteomeXchange with the identifier Project www.doi.org/10.6019/PXD046359.

## Statistical testing

The LC-MS/MS proteome data were log-transformed and analyzed by one-way analysis of variance (ANOVA).

## Ingenuity pathway analysis (IPA)

Networks, functional analyses, and canonical pathways were generated through the use of Ingenuity Pathway Analysis (IPA; Ingenuity Systems, Redwood City, CA, USA) on the list of differentially expressed proteins with value-adjusted $p < 0.05$. Protein symbols were used as identifiers and the user dataset of all identified proteins as background for pathway analysis. For network generation, a dataset containing protein identifiers and corresponding expression values was uploaded into the application. Default settings were used to identify molecules whose expression was significantly differentially regulated. These molecules were overlaid onto a global molecular network contained in the Ingenuity Knowledge Base. Networks of network-eligible molecules were then algorithmically generated based on their connectivity. The functional analysis identified the biological functions and diseases that were most significant to the dataset. A right-tailed Fisher's exact test was used to calculate p values. Canonical pathways analysis identified the pathways from the IPA library of canonical pathways that were most significant to the dataset.

## Co-Immunoprecipitation

To extract proteins, day 0, day 6, day 20 and day 30 stem cell derived left ventricular $HSPG2^{+/+}$ or $HSPG2^{+/-}$ cardiomyocytes were rinsed with ice-cold PBS and treated with RIPA buffer (Thermo Fisher 89900). The cells were then scraped off the dish and incubated for 30 min at 4°C on a rocker. The lysate was centrifuged at 16,000 g for 20 min at 4°C and the supernatant collected. 20 μg of each lysate was incubated with the antibody of interest to immunoprecipitate (a-dystroglycan Proteintech 11017-1-AP; perlecan Thermo Fisher A74; perlecan CCN1 Whitelock et al.,[93] or agrin Santa Cruz 374117) overnight at 4°C. The following day, agarose beads (Thermo Fisher Scientific 20421) were washed with IP buffer (25 mM Tris, 150 mM NaCl, pH7.2), added to the antigen-antibody complex and the mix was gently rotated for 2h at room temperature. The reaction was purified by rinsing the mix with 0.5 mL of IP buffer, centrifuged and the supernatant discarded. This step was repeated two times. To elute the immune complex, 0.5 mL of water was added to the mix, which was then centrifuged, and the supernatant discarded. Electrophoresis loading buffer complemented with SDS (Bio-Rad 1610737) and TPCE (Thermo Fisher Scientific 20490) was added to the eluted immune complex and incubated for 5 min at 95°C. The samples were placed on ice and immediately loaded on SDS-PAGE gels (Bio-Rad Mini-PROTEAN TGX 4–20% Precast Gels) and ran at 150 V for 1 h. Gels were dry transferred using the iblot for 6 min at 20 V. The blots were blocked in 5% non-fat milk/TBS-T and probed with anti-perlecan, anti-agrin or anti-dystroglycan antibodies overnight at 4°C. The following day the blots were washed with TBS-T and incubated with HRP anti mouse/rabbit secondary antibodies for an hour at room temperature before detection using the ECL method.

## Metabolic analysis

### *Seahorse metabolic flux assay*

For Seahorse metabolic flux assay, hPSC-CMs were seeded at 30,000 cells/well of 96 well plate on Seahorse XFp cell culture miniplates (Agilent) to create a confluent monolayer. XFP flux cartridges (Agilent) were pre-hydrated in XF Calibrant (Agilent) overnight at 37°C prior to running assay. One hour prior to measurement, medium was replaced with Seahorse XF DMEM medium supplemented with Seahorse XF Glucose (10 mM), Pyruvate (1 mM) and L-Glutamine (2 mM) (Agilent) and cells were incubated at 37°C in an incubator without $CO_2$ for 1 h. Oxygen consumption rate (OCR) and extracellular acidification rate (ECAR) values were obtained using the

XFp Mito Stress Kit (Agilent). In brief, oxygen consumption rate was measured at baseline, upon oligomycin (2.5 μM), FCCP (2. μM) and rotenone/antimycin (1 μM) injections (Agilent, 103015-100) using the Seahorse XFe96 Analyzer. Data were normalized to the number of cells, as determined by counting DAPI (Thermo Fisher Scientific) stained nucleus using EVOS M5000 imaging system. Maximal respiration was calculated as the difference between FCCP and Rot/AA measurements and spare respiratory capacity was calculated as the difference between maximal and basal respiration.

### Mitochondrial substrate BioLog assay

For mitochondrial substrate functional assessment, we used a previously described protocol optimised for hPSC-CMs.[30] Briefly, MitoPlates (Biolog) were prepared with 30 μL assay buffer mix containing 50 μg/mL Saponin (Sigma-Aldrich) and incubated at 37°C for 1 h. Cells were dissociated, resuspended in 1x MAS Buffer (Biolog) at a concertation of 2x106 cell/mL, of which 30 μL added into each well of the MitoPlate. The MitoPlate was read for 6 h with 5-min intervals at OD590 using a OmniLog plate reader. OmniLog peak value change was calculated via provided software Data Analysis 1.7.

### Image acquisition

Brightfield images were captured using the EVOS7000, higher magnification (x20, 0.7 numerical aperture) images were acquired using Airyscan 2 confocal settings on Celldiscoverer 7 system (Zeiss). Automated image acquisition was performed using the Operetta high-content imaging system (PerkinElmer) on D30 hPSC-CMs.

## QUANTIFICATION AND STATISTICAL ANALYSIS

### Image quantification

Immunocytochemistry relative intensity was quantified using Fiji ImageJ subtracted against background intensity. EHT measurement width was performed using ImageJ measure function taking the average of three measurements at each EHT pole and center. Western blots were quantified using ImageJ intensity on each band, normalized against Revert Total Protein stain lane intensity values. Finally, to quantify multinucleation, images taken by the Operetta high-content imaging system (PerkinElmer) were analyzed (>30,000 cells/per condition), using Harmony high-content imaging analysis software, with an algorithm developed for the determination of cardiomyocyte multinucleation.[35] This algorithm can distinguish between mono-, bi-, and multi-nucleated cardiomyocytes, with its parameters described in detail elsewhere.[36]

### Statistical analysis

Statistical analysis was performed using one-way Anova followed by Tukey post hoc test for timeline results. Individual comparisons were analyzed using unpaired t-tests. Mitoplate substrate comparisons between lines were performed using multiple t test corrected for multiple comparisons by controlling the false discovery rate using Two-stage linear step-up procedure of Benjamini, Krieger and Yekutieli. Results with p values $p < 0.05$ were considered statistically significant. Data are expressed and plotted as the Mean ± SEM or Mean ± SD as indicated in figure legends and results. The sample size used in each experiment is indicated in the figure legends. Statistical analysis was performed using GraphPad Prism 5.0 and RStudio.